Direct ageing of LPBF Al-1Fe-1Zr for high conductivity and mechanical performance

Camille Pauzon, Maxence Buttard, Arthur Després, Frédéric Charlot, Marc Fivel, Béchir Chehab, Jean-Jacques Blandin, Guilhem Martin

Published in

Acta Materialia: doi.org/10.1016/j.actamat.2023.119199

Direct ageing of LPBF Al-1Fe-1Zr for high conductivity and mechanical performance

Camille Pauzon[a,*], Maxence Buttard[a], Arthur Després[a], Frédéric Charlot[b], Marc Fivel[a], Béchir Chehab[c], Jean-Jacques Blandin[a], Guilhem Martin[a]

[a]Université Grenoble Alpes, CNRS, Grenoble INP, SIMaP, 38000, Grenoble, France
[b]CMTC Consortium des Moyens Technologiques Communs, 38402, Saint-Martin d´Hères, France
[c]Constellium Technology Center, Parc économique Centr'Alp, 38341, Voreppe, France

*Corresponding author: camille.pauzon@simap.grenoble-inp.fr

ABSTRACT

The novel Al-1Fe-1Zr alloy leverages the non-equilibrium solidification conditions characteristic of the laser powder bed fusion (LPBF) process, namely a high thermal gradient (G) and solidification front velocity (R). The multiscale characterization of its microstructure in as-built and peak-aged conditions by SEM, TEM with EDS and automated crystal orientation mapping (ACOM), brings new insights on alloy design for LPBF. The solidification conditions permit the solute supersaturation of Fe and Zr, with the latter precipitating as $L1_2$-Al_3Zr nanoparticles following ageing, bringing a high strengthening contribution. In conventional Al alloy ingots, Fe tends to create coarse particles which are detrimental to ductility. Here the Fe particles show a fine globular morphology in the as-built condition, and fine faceted Fe-rich intermetallics are obtained upon ageing. Nanoindentation and in situ tensile tests in the SEM coupled with microscale strain measurements shed light on the relation between microstructural and strain heterogeneities in the as-built condition. Our characterization results for this new Al-1Fe-1Zr grade are synthesized into a simple model for its solidification upon LPBF. In particular, the origin of melt pool boundaries is revealed. These are associated with Fe depletion caused by an early planar growth front, and the evolution of these zones upon ageing is presented. With a high potential for industrial applications, the novel alloy with the two elements Zr and Fe exhibiting low solubility at equilibrium and diffusivity in the Al matrix permit to achieve high conductivity (27 MS/m) and yield strength (330 MPa) after a simple direct ageing step at 400°C/4h.

Keywords: Additive manufacturing; Laser powder bed fusion; Alloy design; Aluminium alloys; Nanoindentation; In situ tensile test; Electrical conductivity.

1. Introduction

Due to lower cost and weight, aluminium is often preferred to copper for electrical and thermal conductors [1]. Additive manufacturing (AM) and in particular laser powder bed fusion (LPBF) allows highly complex geometries to be produced leveraging the excellent conductivity of aluminium [2–5].

Among the most interesting Al alloys with a good strength and conductivity balance, the 6xxx series with Mg and Si additions (after a T6 treatment) unfortunately suffers from poor LPBF processability with a high susceptibility to hot cracking [6–8]. Various approaches were proposed to modify these systems and optimize process parameters to circumvent the issue, such as: addition of inoculating agents (TiB_2, TiC) [6,9–11] or primary phases (the chemically ordered $L1_2$-Al_3X phases with X=Zr, Sc, Ti and a fcc- $L1_2$ structure) [11–16] to promote the heterogeneous nucleation and the formation of finer grains which accommodate thermal strains better; favouring elements that do not extend the solidification range; high temperature powder bed preheating [17]. With mixed success, challenges remain associated with solute evaporation, in particular that of Mg during laser processing, and time-consuming post-processing heat treatments including solutionizing and quenching. Recent work on the development of Al alloys for high mechanical and thermal performances highlight the need for disruptive alloy design strategies for LPBF, allowing to address productivity and sustainability growing demands [18].

Material conductivity is sensitive to alloy composition and microstructure [19,20]. It is determined by the scattering of electrons by disturbances on the crystal lattice structure which can be crystal defects, thermal vibrations, and solute atoms [21]. A good conductivity in aluminium can be obtained by adding elements with very low solid solubility in the cubic matrix. In turn, alloying elements can be selected to fulfil this requirement and contribute to precipitation strengthening. Low diffusivity in the matrix is also an asset to control both in situ precipitation and the ageing response. With this in mind, Fe appears to be an interesting candidate alongside the already popular addition of Zr.

From the ingot metallurgy point of view, Fe in Al alloys is considered detrimental pollution and is a closely monitored impurity. One exception is its addition in the 8xxx series alloys to control the grain size, increase strength and creep resistance [22]. Still, suffering from its poor reputation, Fe has often been disregarded when designing Al alloys for other processes such as AM, despite the recent work of Qi et al. [23] on binary Al-Fe and that of Pérez-Prado et al. [24] on the ternary Al-5Fe-6Cr. With a very low solubility in the Al matrix, the harmful influence of Fe in ingots is attributed to the formation, readily upon solidification, of coarse Fe-rich intermetallics [25,26]. These exhibit faceted and needle-shape morphologies causing loss of strength and ductility. To cope with Fe impurities in Al ingots and push the limits of recyclability, proposed strategies consist in: adding Mn and/or Si to favour the formation of intermetallics with a less detrimental - so-called Chinese script - morphology [27], improving the melt quality to decrease propensity to form oxide films in the melt that can promote intermetallic nucleation [28] (e.g., with ultrasonic casting), and increasing the cooling rate upon solidification. Enhanced cooling rates have also shown to be promising to refine Fe intermetallics in Al-Mg and Al-Cu castings and thereby inhibit their detrimental influence [27]. Fortunately, during LPBF, Glerum et al. [29] showed with operando X-ray diffraction during processing of an Al-Sc-Zr ternary alloy that the cooling rates are in the order of $7\text{-}8\cdot10^5$ K/s, which is very promising for the refinement of possible

intermetallics formed upon solidification, and the restoration of Fe as a desirable alloying element.

The present work provides new understanding on the microstructure development and mechanical and thermal performances of an Al-1Fe-1Zr alloy, whose design solely targets the LPBF processing route. The multi-scale microstructural and mechanical characterization with SEM, ACOM (automated crystal orientation mapping) in the TEM coupled with EDS mapping, nanoindentation, macro-tensile testing and in situ tensile testing in the SEM, sheds light on the realization of this new alloy design and the beneficial role of Fe and Zr as alloying elements in the context of Al alloys processed by LPBF.

2. Materials and methods

2.1. Powder feedstock and LPBF fabrication

The Al-1Fe-1Zr powder was produced by gas atomization, with a particle size in the range of 25.2 µm (D_{10}) to 65.6 µm (D_{90}) and a mean particle size of 42 µm (D_{50}), an apparent density of 1.27 g/cm^3 according to ISO 3923/1 and a Carney flowability of 15 (s/50g) according to ASTM B964 [30]. This feedstock was supplied by Constellium under the trademark Aheadd® CP1.

This powder was loaded in an EOS M290 (EOS GmbH) equipped with a Yb-fiber laser and a 100 µm spot size, offering a building area of 250×250 mm^2. The baseplate made of 5XXX type Al alloy was preheated to 100°C for production. The laser melting was conducted with a 370 W laser power, a 1400 mm/s scanning speed, a 130 µm hatch distance and a 60 µm layer thickness. A striped pattern was applied and rotated by 67° between successive layers. The construction included 6 cubes of dimensions 30×30×30 mm^3, 4 blocks of 60×60×10 mm^3 and 40 cylinders of 10 mm diameter and 60 mm length, all built vertically. The density of the produced material was measured by X-ray computed tomography using a EasyTom Nano-XL system from RX Solution. A sample with a 1 mm diameter was machined to achieve a resolution of 1.1 µm and the relative density was estimated to be of 99.92%. The minimum equivalent radius of detected defects is of 2.9 µm. A 3D rendering of the porosity realized with the Avizo software is available in **Fig. S1**.

Table 1 gives the composition of the virgin gas atomized powder and that of the LPBF printed material. Overall, the laser melting process is associated with very minor changes in content of alloying and impurity elements.

Element	Virgin powder (wt. %)	Bulk LPBF sample (wt. %)	Method
Al	Balance	Balance	N. A.
Fe	1.04	0.997	ICP
Zr	1.17	1.14	ICP
O	0.09	0.08	LECO
H	0.0010	0.0005	LECO

Table 1: Chemical composition in wt.% of the Al-1Fe-1Zr gas atomised powder, measured by inductively coupled plasma optical emission spectrometry (ICP) and carrier gas hot extraction (LECO).

A direct ageing treatment at 400°C with different holding times was investigated. In addition, the impact of a stress-relief consisting of 2h at 300°C was examined. Additional samples for

mechanical testing were heat treated at 400°C for 4h corresponding to the peak-aged condition, determined by Vickers hardness measurements.

2.2. Microstructural characterization

X-ray diffraction (XRD) was performed to detect the presence of phases in the as-built and aged specimens, using a PANalytical X'Pert Pro MPD diffractometer with a Cu source (1.5041 Å), scanning between 12° and 52°, with a 0.026° step size, a scan step time of 900s, and 1D detector. The ICDD PDF4+ database was used for phase identification (**Fig. S2**).

The microstructures were examined with a scanning electron microscope (Zeiss Gemini SEM 500 FEG) equipped with an electron backscattered diffraction (EBSD) detector. The samples of interest were polished until a 1 µm diamond suspension and a final vibratory polishing step with a VibroMet^{TM} 2 from Buehler for 4h using a 0.06 µm colloidal silica suspension. EBSD maps were collected with a 300 nm step size at 20 kV. The toolbox MTex in MATLAB [31] was used for plotting and computing grain sphericity, which is herein defined as the ratio of the grain area to the product of the perimeter and equivalent radius (and therefore equal to 0.5 for a perfectly circular cross-section). The software ImageJ was also employed to perform image analysis such as intermetallic fraction measurement [32].

Additional transmission electron microscopy (TEM) was performed on a TEM FEG JEOL 2100 equipped with energy-dispersive X-ray spectroscopy (EDS) operating at 200 kV for automated crystallographic orientation mapping (ACOM), and on a TEM LaB6 JEOL 2100 for conventional imaging. The TEM lamellae were mechanically ground and polished until a thickness not more than 100 µm, from which 3 mm disks were extracted and electropolished using a solution of 35% nitric acid and 65% methanol at -30°C and 15V.

The ACOM was conducted using ASTAR^{TM} software to retrieve phase and crystallographic orientation information at the melt pool scale and below. This technique is presented in detail in [33] and has been applied successfully to LPBF microstructures, see e.g. [34–37]. The quasi-parallel electron beam with a spot size of about 1 nm on the TEM lamella was scanned over a region of interest. The nanodiffraction patterns were collected in each location as the beam moved across the area with a 2 nm step size. A 1.2° precession of the electron beam was applied, allowing to smooth out the dynamical signals in the record patterns, and thus enhancing the kinematical one, thereby improving the quality of phase indexing [33]. The phase reliability index R can be overlaid on the patterns and permits to compare the correlation of the two best candidate solutions. Typically, when R is greater than 15, the identified solution can be considered by far the best solutions among all the candidates [33]. The candidate phases for the template matching operation performed on the local nanodiffraction patterns by the ASTAR software were defined based on Thermo-Calc calculations and XRD measurements.

2.3. Characterization of properties

At the macroscopic scale, hardness and tensile tests were performed. The Vickers hardness measurements were conducted with a Wilson Tukon 1212 Vickers Tester with a load of 1 kg (HV1). The average and standard deviation of 10 to 15 measures are reported. Macroscopic tensile testing was performed at room temperature on a DY 35 testing machine from ADAMEL with a constant strain rate equal to 10^{-3} s^{-1} and a 20 kN load cell. Cylindrical dog bone specimens with a diameter of 4 mm and 25 mm gauge length, were extracted along the

building direction of the as-built cylinders, to be tested as such and in the peak-aged condition (4h at 400°C). A minimum of 3 specimens per condition was tested.

At the melt pool scale, to study the effect of the hierarchical microstructure obtained from the process, nanoindentation and in situ tensile tests in the SEM were performed. The nanoindentation maps were collected at room temperature using a Berkovich indenter tip on the as-built and peak aged samples. A UNHT3 Anton Paar system was employed under a constant strain rate loading of 0.05 s^{-1} until a maximum depth of 75 nm. The local indentation hardness (H_{IT}) was obtained with the Oliver and Pharr method [38], in 600 and 1000 points on the as-built sample and heat treated one at 400°C for 4h, respectively. The analysis of the probed areas was completed by SEM and EBSD analysis.

The in situ tensile testing in the SEM at room temperature were performed on the as-built and peak-aged conditions. Specimens were extracted from the as-built 30×30×30 mm^3 cubes by electro-discharge machining. A Gatan Microtest micro-tensile stage mounted within the SEM was used with a 2 kN load cell, as presented in more details by Dessolier et al. [39]. As this micromechanical device only works in displacement control, a LabView interface developed in-house adjusting the displacement throughout the test was used. It permits to achieve a quasi-constant strain rate of 10^{-3} s^{-1}. Prior to tensile testing, an area within the gauge length of each sample was selected and characterized with SEM. For the starting condition and the subsequent loaded stages, high-definition BSE images of 8192 × 6144 pixels were taken at a ×1000 magnification, thereby achieving a resolution of 13.96 nm/pixel. To achieve a high signal to noise ratio, low scanning speeds were chosen, leading an acquisition time of about 20 minutes per frames. The brightness and contrast settings were optimized to achieve the broadest distribution of the grayscale histogram. The post-processing of the acquired stages and the determination of the in-plane deformation was performed with the CMV software as conducted in [40–42]. A 300×300 pixels correlation subset was used (i.e., 3.9 × 3.9 μm^2). The plotting of the computed local deformation was performed with in-house Python routines. In addition, for the nanoindentation and in situ tensile tests, distributions of hardness and deformation were plotted using Python scripts and Kernel Density Estimation (KDE) [43], with a bandwidth of 0.4.

The electrical conductivities were measured by the Eddy current method with a NORTEC 600C apparatus from Olympus, using a 20 mm diameter probe operating at 60 kHz. Two calibration samples were employed for the initial adjustments with 17.37 MS/m and 34.56 MS/m. When needed, the electrical conductivity was converted into thermal conductivity using the Smith-Palmer relationship [21].

2.4. Thermodynamic calculations

Calculations of solidification path at equilibrium and using the Scheil-Gulliver model were performed with Thermo-Calc version 2022b using the TCAL6 Al-Alloys v6.0 database (**Fig. S2**). Combined with XRD and literature survey, these calculations support the establishment of the candidates list for the ACOM analysis of the studied alloy system. The assumptions of the Scheil Gulliver model, which are infinite diffusion in the liquid, no diffusion in the solid and equilibrium at the solid-liquid interface, are considered to be most representative of the LPBF process conditions. One should bear in mind it neglects solute trapping and back-diffusion in the solid. Still, it permits to predict the phases forming and the composition of the liquid and matrix upon solidification. Additional equilibrium phase diagram is calculated to estimate Fe and Zr solubilities in Al, phase fractions and their compositions at equilibrium.

3. Results

3.1. Hardness, electrical conductivity and macroscopic tensile behavior

The evolution of hardness and electrical conductivity with respect to ageing time at 400°C was studied, see Figure 1a-b). In addition, the influence of a post-fabrication stress-relief heat treatment of 2h at 300°C, as conducted in [18], was considered when applied before the 1h, 4h and 7h ageing treatments at 400°C, and also compared to the as-built state.

It is first noted that the as-built and stress-relief materials have the same hardness (HV1 = 67 kgf/mm^2), while the conductivity of the stress-relief one is slightly higher (18 MS/m vs. 17 MS/m). This highlights slight onset of solid solution changes within the stress-relief sample. This minor difference in conductivity is also observed after 1h at 400°C (19 MS/m for the sample subjected to direct ageing 400°C/1h vs. 20 MS/m for the sample subjected to SR+400°C/1h), but it becomes negligible after 4h at 400°C (26.5 MS/m). On the one hand, the peak ageing appears between 4h and 7h. Indeed, the hardness does not seem to vary between 4h and 7h at 400°C but then drops for longer ageing times. On the other hand, the conductivity of 26.5 MS/m after 4h/400°C, continues to increase after 7h for extended ageing time as the solid solution is more and more depleted in solute atoms (30 MS/m after 400°C/96h). Consistently, the microstructure of the sample aged 96h reveals the extensive coarsening of intergranular Fe-rich precipitates (**Fig. S3**).

These results highlight that the slightly higher conductivity of the SR sample compared to the as-built one, is retrieved by the directly-aged specimens after 4h at 400°C. This is promising to reduce the post-processing time of the LPBF components. For instance, one could imagine performing direct ageing at 400°C for bulky and complex-shaped components while these are still on the baseplate in order to avoid part warping. The measured electrical conductivity after 4h/400°C permits to estimate the thermal conductivity to be about 180 W/m·K using the Smith-Palmer law [21].

Based on Vickers hardness and conductivity evolutions, the conditions as-built and directly aged at 400°C for 4h were selected for more advanced characterization. The tensile responses of representative as-built and peak-aged (400°C/4h) samples are displayed in Figure 1c-e), alongside the derived tensile properties in Table 2. Similar yield strength levels and elongations are obtained to those reported for stress-relieved (i.e. $YS_{0.2\%}$ is about 135 MPa and %A ~ 18%) and peak-aged specimens in [18] ($YS_{0.2\%}$=330 MPa, %A ~ 15%), demonstrating the robustness of the processability of the designed Al-1Fe-1Zr alloy. As strength increases from the as-built to the peak-aged condition by about 100%, ductility reduces slightly. One can note distinct work hardening extents and rates between the two conditions in Figure 1e, which shall be investigated in future work.

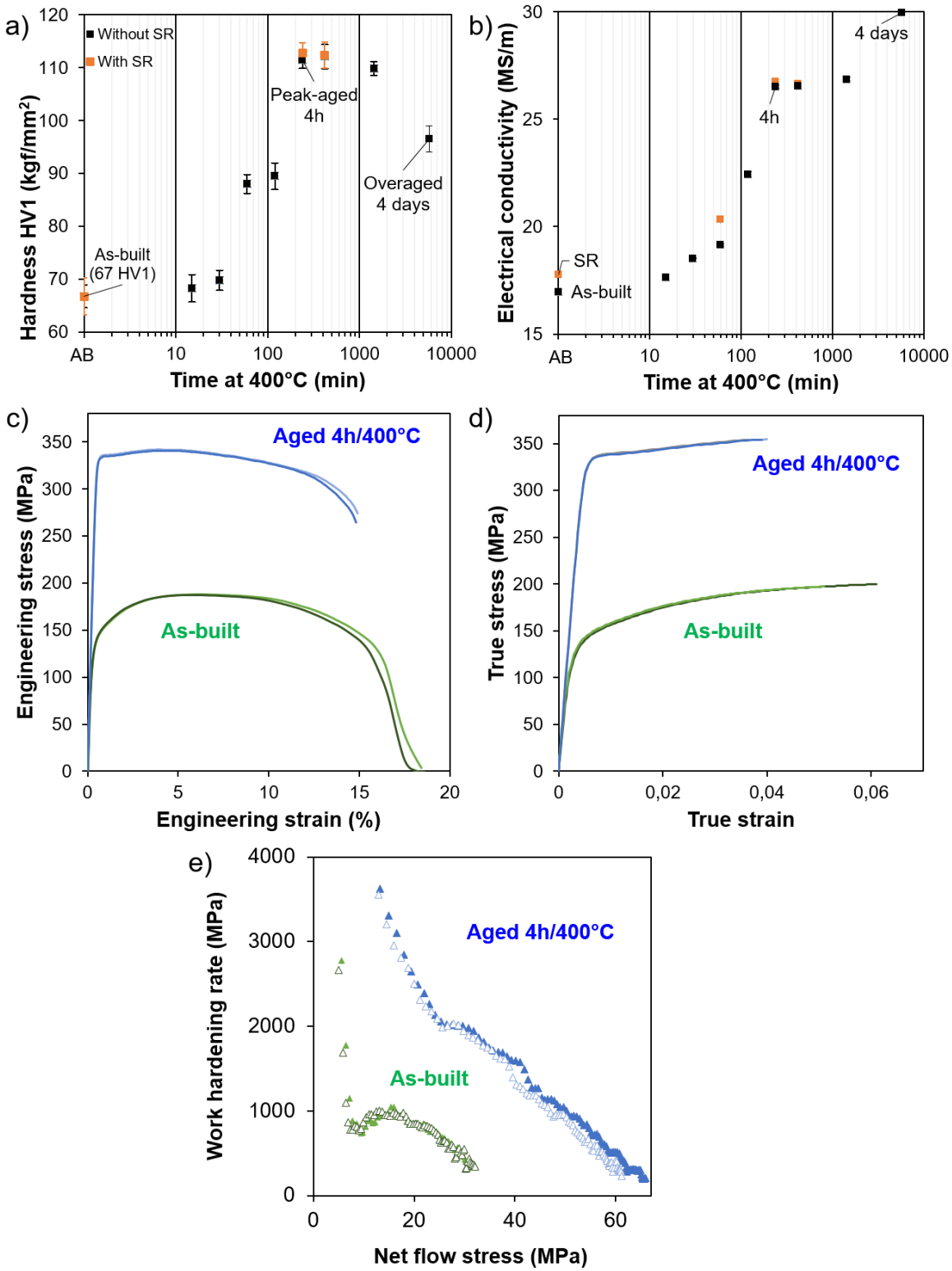

Figure 1: a) Evolution of hardness (HV1) and b) electrical conductivity as a function of ageing time at 400°C, with and without stress-relieving (SR) at 300°C for 2h. c-d-e) Typical engineering and true tensile curves of the the LPBF-produced Al-1Fe-1Zr alloy in the as-built and peak-aged conditions. e) Work hardening rate as a function of the net flow stress (substraction of the true yield strength from the true stress). The results for two samples representative of the tested batches are displayed for clarity.

Table 2: Tensile properties of the Al-Zr-Fe LPBF alloy extracted from Figure 1c)-d). $YS_{0.2\%}$ is the yield strength, Rm is the engineering tensile strength, UTS is the true ultimate tensile strength, A is the elongation at failure measured on the engineering tensile response, and the Au is the uniform elongation measured on the true stress-strain curves based on Considere's criterion. for necking. 3 tensile tests for each condition are reported.

Condition	$YS_{0.2\%}$ (MPa)	Rm (MPa)	UTS (MPa)	A (%)	Au (%)
As-built	134-137	187-188	197-200	18.0 – 18.4	5.2 – 6.3
4h/400°C	334-337	340-342	355-357	14.8 – 15.0	3.7 – 4.1

3.2. Microstructure of the as-built and aged alloy

The typical bimodal grain distribution for this alloy processed by LPBF is obtained with fine equiaxed and columnar grain zones (FEZ and CZ, respectively), as seen in Figure 2a) and d), and as reported in [18]. At this scale, the grain structure appears stable following the ageing heat treatment at 400°C. With a sphericity index threshold of 0.35, the FEZ represents a minor fraction of all the grains of about 2% for the as-built and the aged 4h/400°C conditions (**Fig. S4**). Grains of the FEZ have diameters of about 1 µm, while those in the CZ are typically few micrometers in width and between tens to several hundred micrometers in length.

BSE images reveal the presence of intermetallic particles within and at the grain boundaries with bright contrast, previously identified as $Al_{13}Fe_4$ in the stress-relieved and aged material [18], see Figure 2b-c) and e-f). Additional SEM EDS maps provided in supplementary **Fig. S5** confirms that the grain boundary particles are enriched in Fe. In the as-built state, these particles appear with a globular morphology and represent a surface fraction of about 6% measured with ImageJ. No significant variations in size of these particles were observed across the solidified melt pool (**Fig. S6**). In the aged state, additional particles with faceted aspect are formed. A total fraction of Fe-rich particles of about 9% is measured using ImageJ after ageing at 400°C for 4h. Both values are likely overestimated since Thermo-Calc reports a volume fraction of 1.8% (atomic fraction of 2.2%) of $Al_{13}Fe_4$ under equilibrium conditions.

The combination of EDS and ACOM provides with local chemical, phase, and orientation information. As depicted in Figure 3a-c), it is confirmed that the alloy is characterized by globular $Al_{13}Fe_4$ intermetallic particles formed upon solidification of average diameter 50 nm (measured on SEM-BSE images with ImageJ) composed of many nanocrystals as shown in [18], and faceted $Al_{13}Fe_4$ that have precipitated upon ageing at 400°C, up to hundreds nm in length as seen in Figure 2f). The minor presence of Al-rich oxides is also noted. One can also observe that globular $Al_{13}Fe_4$ intermetallic particles present at the grain boundaries have experienced growth and coarsening upon ageing, which is particularly visible within the FEZ where grain boundary density and diffusion enhances this phenomenon, see Figure 2e). In contrast, the intragranular globular $Al_{13}Fe_4$ do not appear to have changed in size upon ageing for 4h at 400°C.

Next to the ACOM orientation map are displayed nanodiffraction patterns of the Al matrix and of the two types of Fe-rich particles. The local matched templates of the best candidate phases are displayed as well as their corresponding R index. Despite the reliable solutions (R > 14), numbers of diffraction spots are not corresponding to the best candidate

phase template, but instead to the surrounding Al matrix. This is because the small precipitates are embedded in a large volume of the matrix with a strong diffraction signal.

Dark field TEM image and selected area diffraction pattern (SAED) in 2-beam condition of the peak-aged Al-1Fe-1Zr specimen, reveal the homogeneous precipitation of a coherent nano-sized phase within the Al grains, see Figure 4a-c). Such fine precipitation is not observed in the as-built specimen, which only features scarce amount of coarser primary $L1_2$-Al_3Zr particles resulting in the formation of the FEZ (**Fig. S7**). The fine coherent precipitation observed in the 4h/400°C aged material is identified as $L1_2$-Al_3Zr nanoprecipitates, similar to that obtained through ageing of LPBF Al alloys containing Zr [11,44], or Sc and forming Al_3Sc [45,46]. A dark field image obtained from the selection of the $L1_2$-Al_3Zr superlattice reflection is displayed in Figure 4c). It corresponds to a magnified region of the BF image in Figure 4a). The fine dispersion of nano $L1_2$-Al_3Zr stands clearly with bright contrast. A local depletion in these particles is evident at the vicinity of the Fe-rich globular particles depicting precipitate free zones (PFZ). This is consistent on the one hand with the peritectic nature of Zr, and on the other hand with the lower amount of vacancies in regions adjacent to the interface between the Fe-rich intermetallic and the matrix resulting in reduced Zr diffusion and thereby limited nano $L1_2$-Al_3Zr precipitation. Indeed, vacancies are preferential sites for precipitate nucleation and grain boundaries are acting as vacancy sinks [47,48].

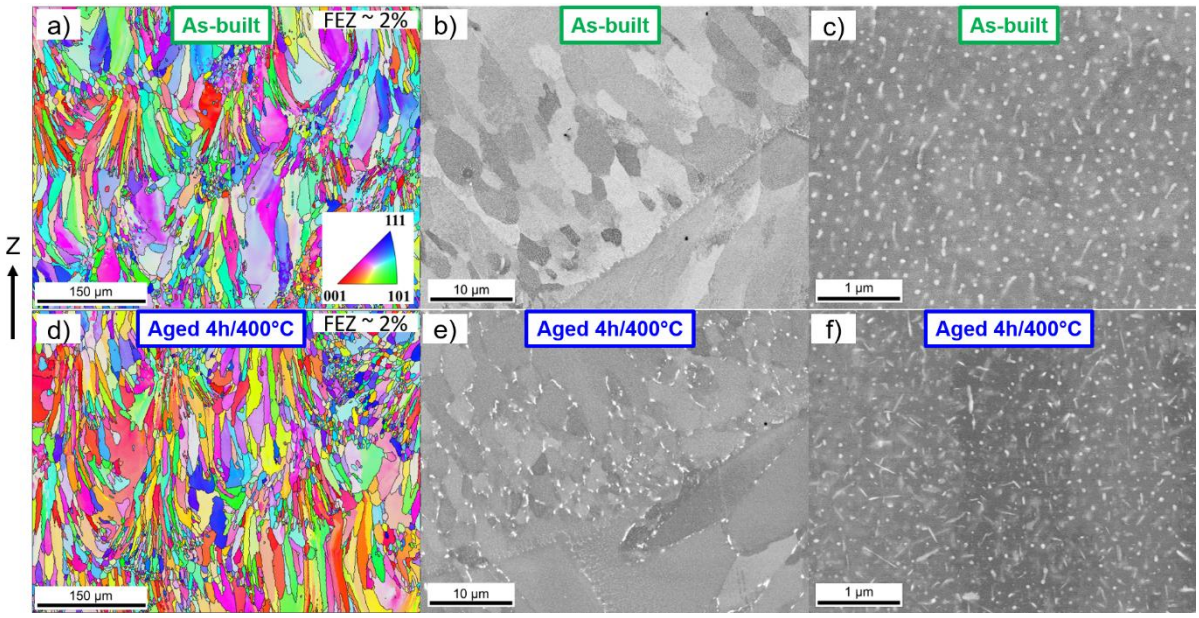

Figure 2: EBSD orientation maps in inverse pole figure (IPF) colouring along the building direction (Z) for a) the as-built material, and d) the aged one at 4h/400°C. BSE images at the melt pool scale b-e), and within the columnar grains c-f), for the as-built and the aged material.

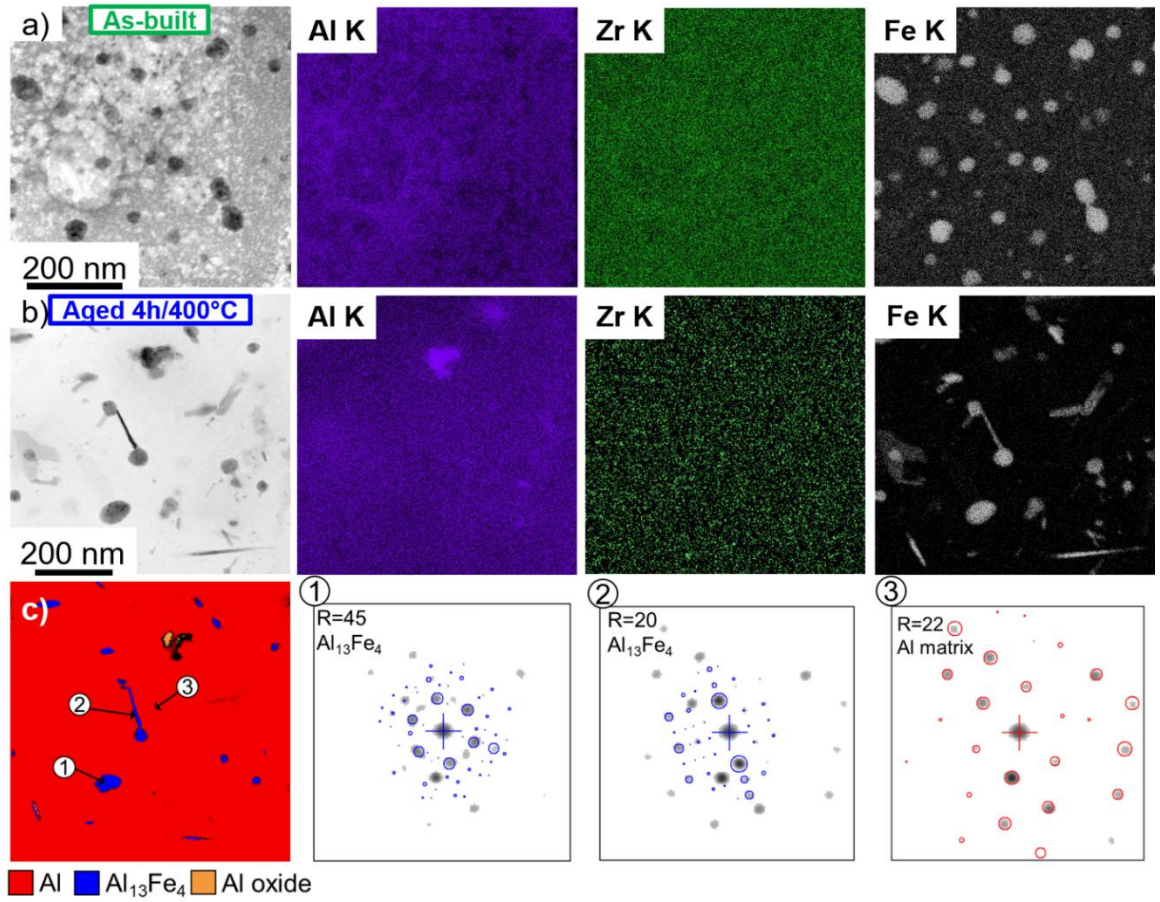

Figure 3: Bright Field STEM images and EDS maps of Al, Zr, and Fe for a) the as-built and b) the directly aged material at 400°C for 4h. c) Corresponding ACOM phase map for the aged sample, showing the morphology and distribution of phases identified with ASTAR™. The phase reliability (R) is overlaid in grey scale on the map. Selected nanodiffraction pattern alongside their R index are displayed. For precipitates, inserts show the overlaid matrix mask highlighting the strong diffraction signal of the matrix.

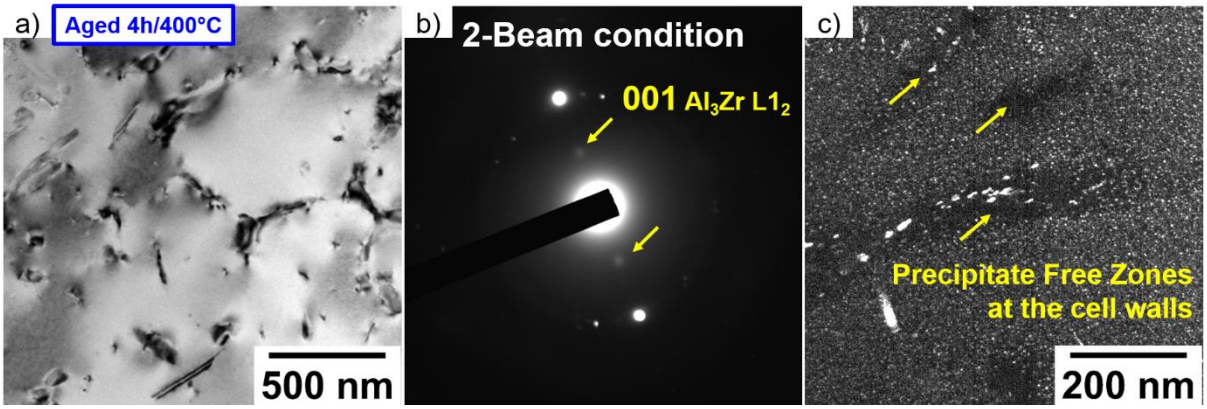

Figure 4: Precipitation of nano $L1_2$-Al_3Zr precipitates in the directly aged material at 400°C for 4h: a) BF TEM image where Fe-rich particles have a dark contrast, b) SAED pattern collected in 2-beam condition where superlattice reflections of the coherent nano Al_3Zr particles are pointed out, c) DF image in the region of interest from the $L1_2$-Al_3Zr reflection selection depicting PFZ at the cell walls.

3.3. Melt pool boundaries (MPBs)

A closer examination of the microstructure at the melt pool scale reveals the presence of distinct melt pool boundaries (MPBs), underlined with yellow dashed lines in Figure 5a). Unlike other LPBF Al alloys benefiting from the role of inoculants [34], it can be noted that these MPBs do not always coincide perfectly with the appearance of the FEZ but are shifted several microns underneath, see Figure 5c). In some areas, the cross-section shows the MPB without any associated FEZ.

In addition, the MPBs seem to be connected to both a change in grain growth direction and local intragranular misorientation along the MPBs. The first aspect, grain growth direction change, is clearly observed within the purple-oriented grain in the bottom left section of the EBSD map in Figure 5b). The second feature, intragranular misorientation, is particularly distinguishable on the EBSD map for the uppermost MPBs, see the corresponding area pointed out by the yellow arrow in Figure 5a). This local misorientation was more clearly evidenced using the orientation map collected with ACOM on a TEM lamella over a MPB, see Figure 5d-e). At this MPB, the misorientation is of about 3.5°, see Figure 5f). The STEM-EDS mapping of the same region of interest reveals that MPBs are also subjected to composition variation and especially an important local depletion in Fe. This result is comparable to what was found by Qi et al. [49] in a Al-2.5Fe alloy also produced by LPBF, with fine Fe-rich intermetallics below the MPB and a network of coarser ones just above. One should emphasize that even after ageing, this zone of a few hundreds of nanometres depleted in Fe, still does not exhibit the presence of faceted $Al_{13}Fe_4$ precipitates (**Fig. S8**). The presence of this Fe-depleted zone at the MPBs of LPBF alloys has not been explained in the current literature. This observation will be rationalized in the discussion section.

With SEM no microstructural changes are visible in these MPBs following the ageing treatment at 400°C for 4h. However, dark field TEM imaging and SAED reveal that these zones underwent the homogeneous nano $L1_2$-Al_3Zr precipitation, see Figure 6, which is also observed in the peak-aged Al-1Fe-1Zr material, see Figure 4. The SAED pattern displays the superlattice reflections of the coherent phase, see Figure 6b), and the DF image reveals the fine precipitation with bright contrast. The nano $L1_2$-Al_3Zr precipitation within this Fe-depleted zone at the MPBs is consistent with the Zr distribution apparent in Figure 5g). In addition, as expected from the Fe depletion noted in the MPB in the as-built condition, no secondary precipitation of Fe-rich particles is depicted upon ageing either by SEM-BSE or TEM imaging.

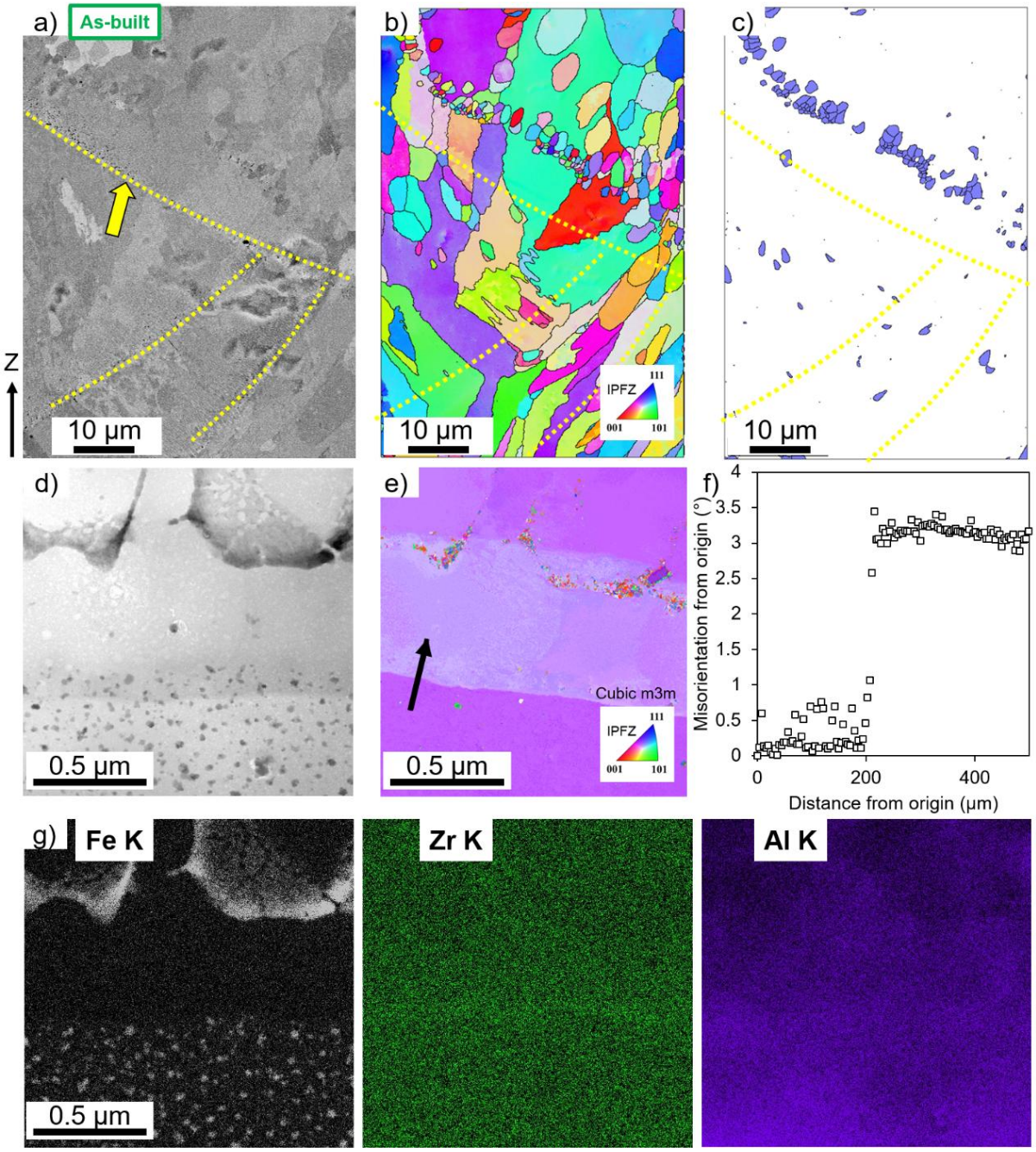

Figure 5: a) BSE image showing several melt pool boundaries, b) Corresponding EBSD orientation map with IPF Z colouring, c) Fine grains from this area considering a diameter below 5 µm and a sphericity index > 0.35, d) STEM BF image of a melt pool boundary, e) Corresponding ACOM orientation map (IPF colour code) in the Z direction, f) local misorientation over the melt pool boundary, g) Fe, Al and Zr EDS maps in the same region of interest.

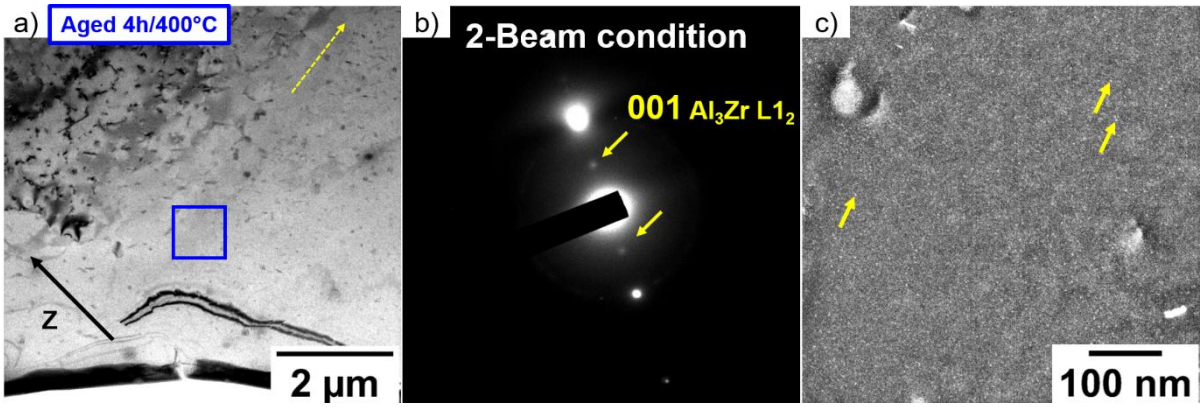

Figure 6: Precipitation of nano $L1_2$-Al_3Zr precipitates within the Fe-depleted region at the MPB of the directly aged material at 400°C for 4h: a) low magnification BF image where the yellow arrow is along the Fe-depleted region at the MPB, the blue frame is within this region of interest; b) the SAED pattern collected within the region of interest in 2-beam condition where superlattice reflections of the coherent nano Al_3Zr particles are pointed out; c) DF image of the corresponding area from the $L1_2$-Al_3Zr reflection selection where selected nano Al_3Zr particles are pointed out. The speckle appearance of this image is owing to the fine nanoprecipitation.

3.4. Mechanical response at the melt pool scale

To further investigate the influence of the hierarchical microstructure obtained from the LPBF process, nanoindentation mapping was conducted at the melt pool scale in the as-built and peak-aged conditions, see Figure 7 and Figure 8.

In the as-built sample, a clear demarcation in the indentation hardness H_{IT} map is visible and coincides with the MPB, see Figure 7c-d). The hardness values appear to be in average 1140 MPa below the MPB and 990 MPa above. This hardness map is displayed next to the corresponding EBSD orientation map of this region. It turns out that the indentation hardness is not having an obvious relationship with the grain size which may be related to the reduced volume probed by the Berkovich tip, see Figure 7b). The hardest region is located at the top of the previously solidified columnar grains or CZ.

In the peak-aged sample, the hardness disparities across the MPB are no longer visible, and both regions, above and below the MPB, have reached comparable average hardness of about 1420 MPa, regardless of the grain size obtained with EBSD, see Figure 8. Overall, the measurements depict a 40% increase from the as-built to the peak-aged state. Locally, the regions above MPBs have experienced a hardness increase of about 45% and the ones below of about 25% following ageing.

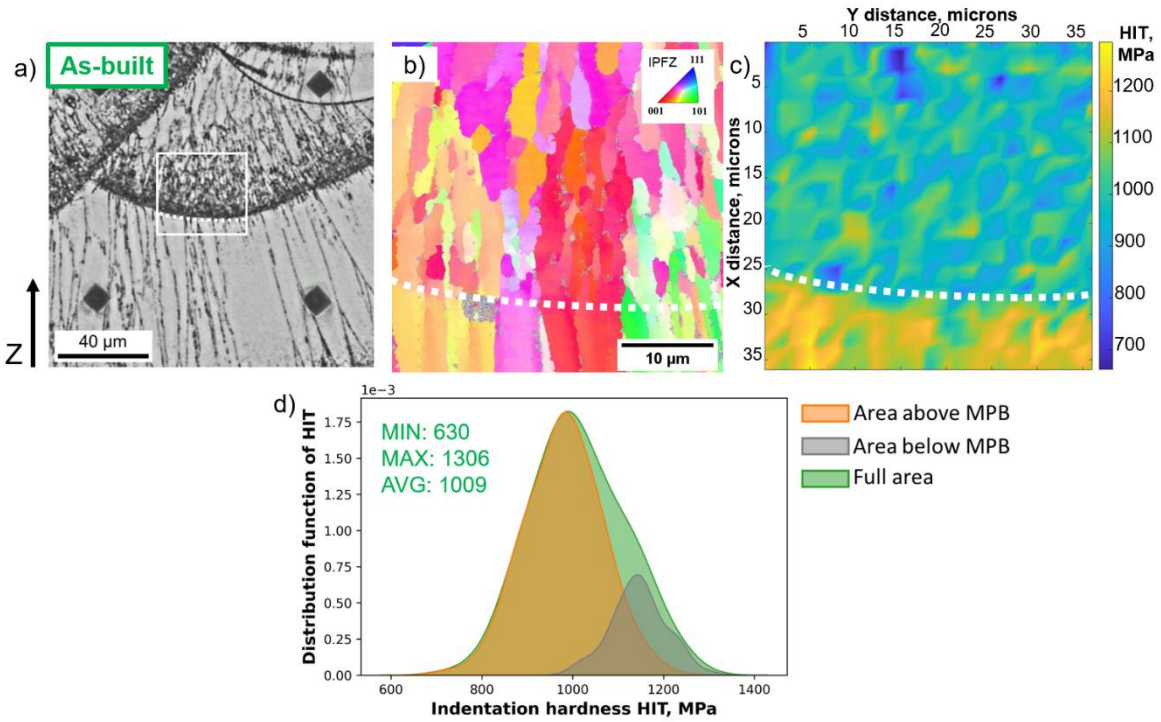

Figure 7: a) Region of interest in the white frame, b) EBSD-IPF map, c) nanoindentation map, and d) H_{IT} distributions in as-built Al-1Fe-1Zr. The MPB is outlined with a white dashed line.

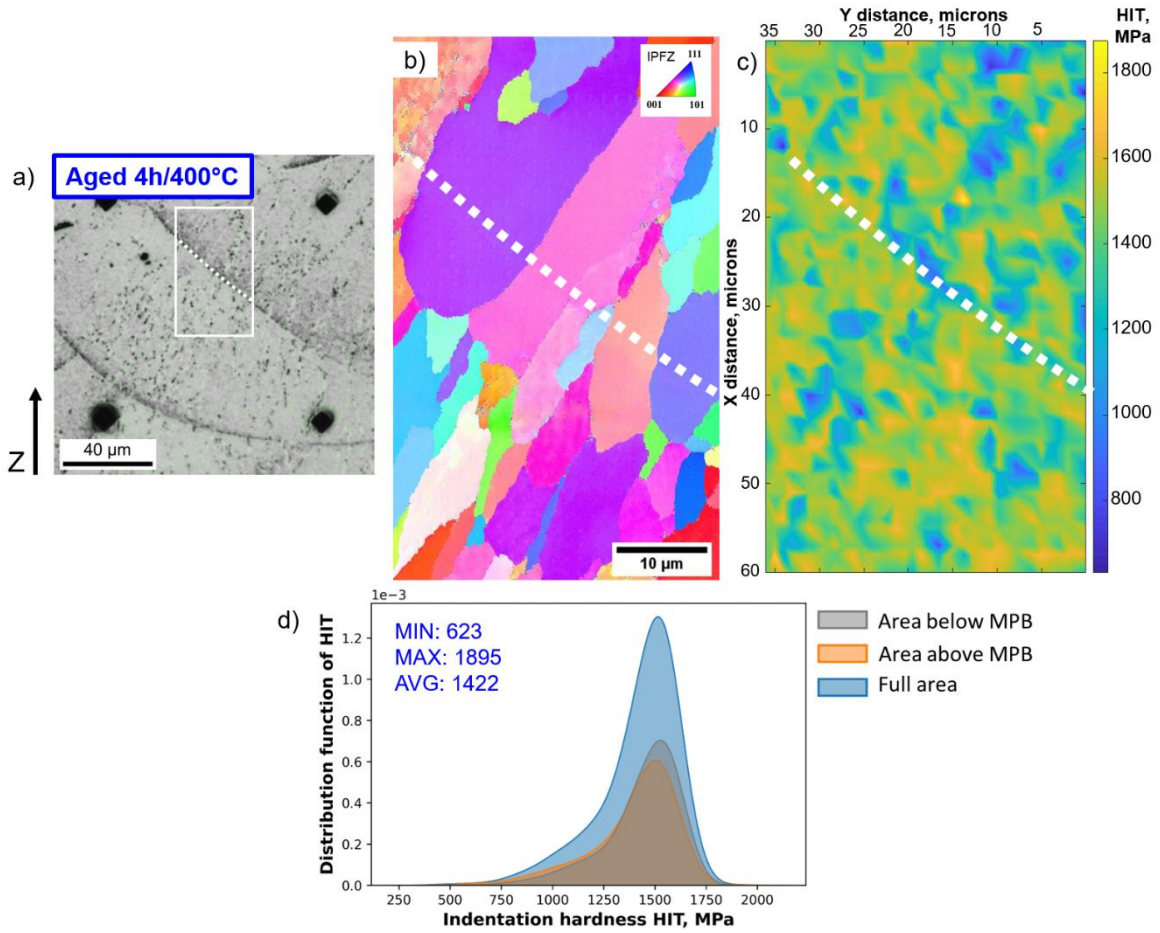

Figure 8: a) Region of interest in the white frame, b) EBSD-IPF map, c) nanoindentation map, and d) H_{IT} distributions in peak-aged Al-1Fe-1Zr. The MPB is outlined with a white dashed line.

The in situ tensile tests of the as-built and peak-aged specimens evidence the presence of local strain heterogeneities, which can be seen as signatures of the local microstructural heterogeneities. To perform these tests, the fine Fe-rich intermetallic particles were used as speckled patterns to be tracked in the high-resolution BSE images of the deformed states using digital image correlation (DIC). Images collected after various strain increments along the tensile curve were recorded. Two steps for both samples are selected and the corresponding normalized tensile strain maps are displayed in Figure 9. The first step is taken shortly after the yield strength ($YS_{0.2\%}$) and the second midway between the $YS_{0.2\%}$ and the onset of sample necking. For each step, the colour maps indicate the magnitude of the local strain normalized by the average tensile strain. In addition, the image of the undeformed microstructure is displayed with BSE contrast and overlaid normalized isostrain lines ($\varepsilon_{11}/\langle\varepsilon_{11}\rangle = 1$) plotted in plain black. The MPBs are also indicated with white dashed lines on the initial microstructures.

For the as-built sample, some regions exhibit local tensile strain 50% above the macroscopic tensile strain already at the first strain step of ~ 1%, see Figure 9a). The isostrain line overlaid on the microstructure permits to observe that one such region is following closely the bottom right MPB of the analysed region. This MPB is connected to two other MPBs close to the centre of the presented frame. An onset of localised strain from the frame centre towards these two lower-left MPBs can also be noted.

Interestingly, high local tensile strains seem to be situated in the analysed frame´s upper part. This could be connected to the lower nanoindentation values typically obtained in these regions, see Figure 7c), and a transmission of the strain localisation from the bottom right MPB to this region. In addition, the influence of the 3D structure of the melt pools on the 2D strain observations should not be disregarded, since localisation can also occur within the sample thickness. Finally, other areas with locally higher strains can be distinguished such as in the bottom-left corner. Once again this may be attributed to a nearby MPB, beneath and/or not in the observed field, for example in the specimen thickness.

At higher macroscopic strain (~ 2.4 %), the strain seems to accumulate at specific locations on the bottom-right MPB, at the centre point where MPBs connect and more diffusely in the upper region, above the MPBs, see Figure 9b).

In the case of the peak-aged specimen, the strain appears more homogeneously distributed across the MPBs, which is in good agreement with the nanoindentation results, see Figure 9c) and Figure 7c). The strain seems to localize in areas where a large density of coarse intergranular Fe-rich intermetallics is observed, see the microstructure within the normalised isostrain lines in Figure 9c). One should underline here that previous TEM analysis revealed such Fe-rich intermetallics can be associated with adjacent PFZ, free of nano $L1_2$-Al_3Zr precipitates, see Figure 4c). A higher density of such PFZ could in part explain the preferential localisation of strain in such zones. For higher macroscopic strain, the deformation continues to localise in these areas, while the rest of the microstructure continues to deform rather homogeneously, see Figure 9d).

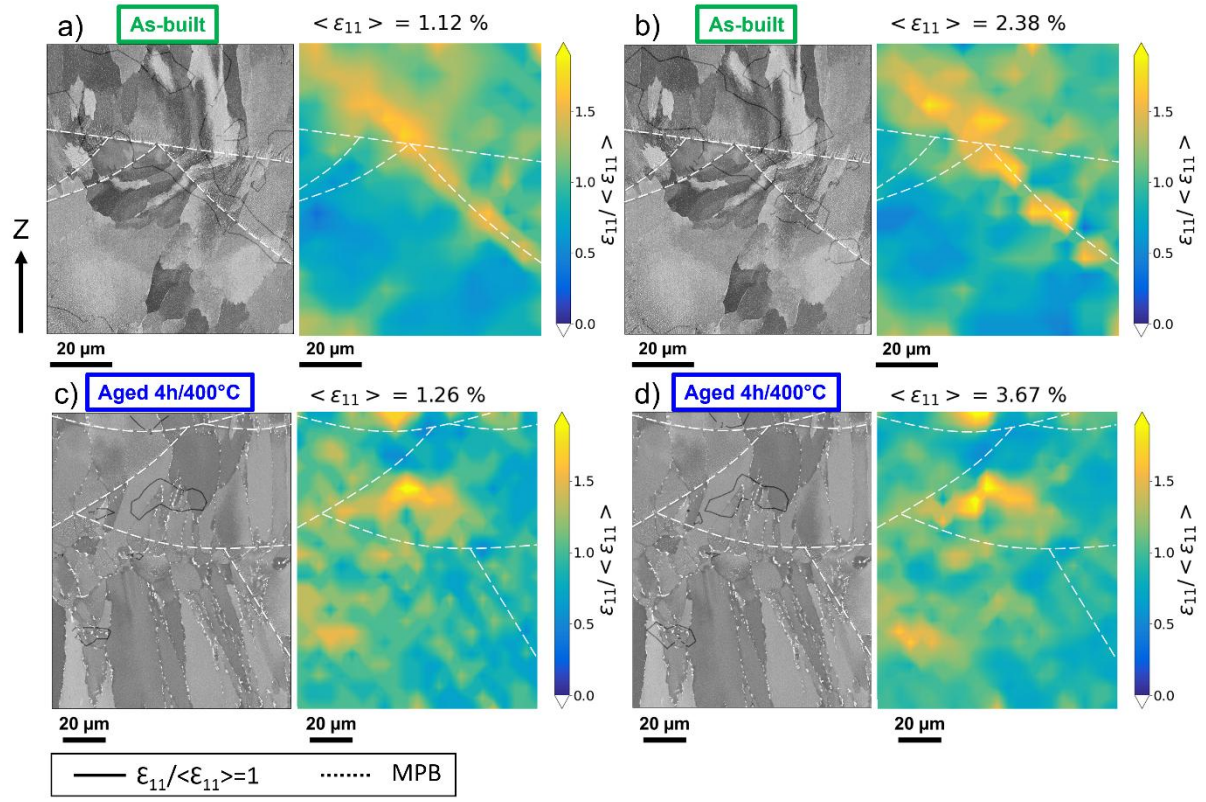

Figure 9: Microstructure of the regions of interest analysed by DIC during in situ tensile testing using BSE high resolution images for a-b) the as-built, and c-d) the peak-aged samples. The MPBs are overlaid in dashed white lines and the isostrain lines ($\varepsilon_{11}/\langle\varepsilon_{11}\rangle = 1$) in black plain lines. The colour maps of the normalized local tensile strains are displayed for

elongation close to the elastic limit and midway to the necking. The loading direction is parallel to the building direction (Z).

To summarize the findings from these tests at the melt pool scale, Figure 10a) and b) display the distributions of the plastic deformation obtained from the in situ tensile tests for the 1st deformation step (with $<\varepsilon_{11}>$ of about 1%), and the nanoindentation hardness distributions for the as-built and peak-aged materials, respectively. The nanoindentation map of the as-built specimen revealed a spatially heterogeneous response (Figure 7c)), while the corresponding statistical distribution appears rather narrow and centered around the average value of 1010 MPa (Figure 10b)). In comparison, the distribution of tensile plastic deformation in the same material is clearly having a bimodal aspect (Figure 10a)). This bimodal aspect is owing to the pronounced localisation of the deformation in the vicinity of the MPBs, see Figure 9a-b). In contrast, the distribution of the normalized tensile deformation in the peak-aged sample is well centered (Figure 10a)). Interestingly, the peak-aged material which appears to have a more homogeneous spatial distribution of indentation hardness as shown in Figure 8c), is characterized by a distribution partly skewed to the left towards low hardness values, see Figure 10b). The cause of this discrepancy is detailed in the discussion section, as well as the heterogeneities of spatial deformation and indentation distribution in the as-built material.

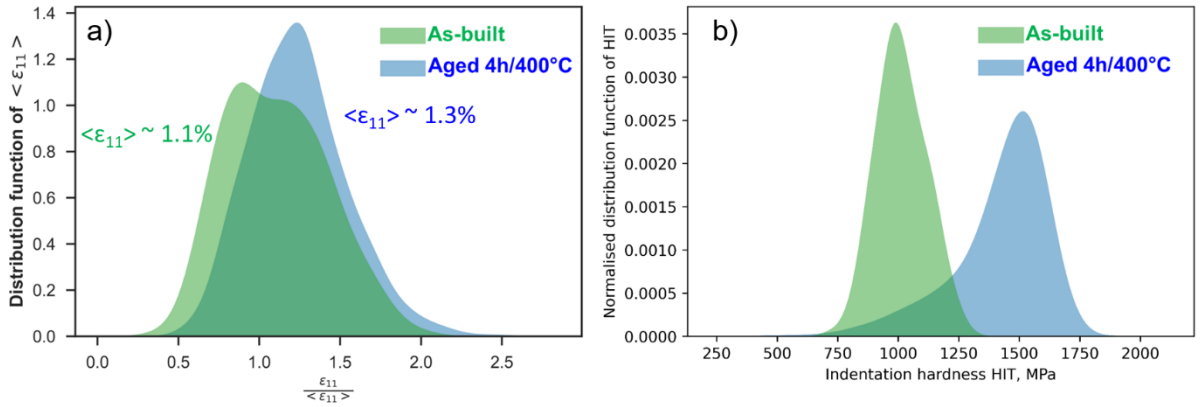

Figure 10: a) Distributions of normalized tensile deformation obtained from the 1st deformation step and determined by DIC, and b) distributions of the nanoindentation hardness for the as-built and peak-aged Al-1Fe-1Zr materials.

4. Discussion

4.1. Alloy performances

An Ashby chart has been proposed to locate the performances of the Al-1Fe-1Zr alloy in as-built and aged conditions with respect to the cast and wrought series as well as relevant other LPBF grades in [18]. This one illustrates how typically conventional Al alloys are either strong or good conductors. The 6xxx series following a T6 heat treatment appears as the only conventional Al alloy family with performances (strength-conductivity trade-off) approaching that of the present grade [50]. However, it suffers from poor LPBF processability. Considering well-established grades for LPBF, the AlSi10Mg in stress-relieved condition permits achieving a YS of 200 MPa for a conductivity of 160 W/m·K [51].

Among other Al-Fe LPBF alloy alternatives for high conductivity, Al-2.5Fe can provide a YS of about 250 MPa and thermal conductivity of about 185 W/m·K after heat treatment of 10h at 300°C, and ductility of about 5% along the building direction [52]. Therefore, the present Al-1Fe-1Zr is particularly interesting to achieve a high strength-conductivity trade-off following a direct ageing treatment (YS of 330 MPa and conductivity of 180 W/m·K), while sustaining interesting ductility and benefiting from LPBF design freedom.

4.2. Solidification at the melt pool scale

The multi-scale characterization of the Al-1Fe-1Zr alloy as well as the confrontation to recent literature permits to assert that the solidification of the melt pool occurs primarily by epitaxial growth for which there is no nucleation barrier. Atoms from the melt deposit on the existing lattice sites of the adjacent solidified grains; while in the melt, primary $L1_2$-Al_3Zr particles form and initiate the heterogeneous nucleation of the Al matrix. Examples of primary $L1_2$-Al_3Zr particles observed within FEZ grains are presented in supplementary **Fig. S7**. These two nucleation and growth mechanisms will eventually impede each other. This is schematically represented in Figure 12 and described in more detail below.

Epitaxial growth: planar to cellular growth front

The solidification conditions, namely the solidification front velocity R (m/s) and the thermal gradient G (K/m), determine the amount of constitutional supercooling and thereby the solidification structure at all locations within the melt pool. These solidification conditions have been studied and modelled for LPBF [53,54] and different welding processes [55,56]. It is rather well-established that the solidification front velocity R is the smallest for 1st solidified liquid. And in contrast, the thermal gradient G decreases from the first solidified liquid to the last.

At the bottom of the melt pool (1st solidified liquid), both minimal R and maximal G conditions are reunited and thereby promote a planar solidification front (no constitutional supercooling), see Stage I in Figure 12. Typically, within the planar growth region no segregation is encountered, while Fe accumulates ahead of the solid-liquid interface (Stage II). This is highlighted by the integrated FeK EDS signal across a MPB displayed in Figure 11, exhibiting a minimal and steady intensity over the width of the planar growth region. In comparison, the ZrK signal exhibits a peak at the beginning of this region, which is discussed below considering partitioning coefficients. Planar growth at the bottom of the LPBF melt pools has been evidenced in the 316L austenitic stainless steel, see e.g. [57]. Herein, the planar growth extends over approximately 500 nm and is observed within the printed material over no more than several hundreds of nm.

As solidification continues, R increases and G decreases, and the constitutional supercooling increases. The local perturbations at the solidification interface are thus amplified and become protrusions aligned with the thermal gradient. As a result, the planar growth interface becomes unstable and a transition to a cellular growth front operates (Stage III). Zhu et al.[58] recall that for laser processes, the instability of the planar growth front may also be promoted by the dynamic melt flow and the vaporization causing pronounced Marangoni flow.

As solidification proceeds, Fe is rejected to the liquid in the lateral regions of the cells, while Zr content is higher at the core cells, see depletion of nano Al_3Zr particles after ageing at the intercellular spaces in Figure 4a). As modelled by Zhang et al.[53] for LPBF of titanium

aluminides, eventually the initial cell structure undergoes adjustments such as cessation, merging and splitting to minimize the interfacial energy, and thereby establishes stable cell tips. The intercellular regions enriched in Fe result in the $Al_{13}Fe_4$ formation. The alignment of the globular Fe-rich particles along the building direction within the CZ is a signature of the stable cellular front growth in that region (**Fig. S9**). This microstructure recalls that observed by Gremaud et al. [59] after laser treatment of Al-2Fe (wt.%), for which the authors underline the spheroidization tendency at the interdendritic spaces. Such globular morphology of the $Al_{13}Fe_4$ suggests a solidification in the CZ similar to divorced eutectic, which is common in hypoeutectic alloys with low solute amount [60].

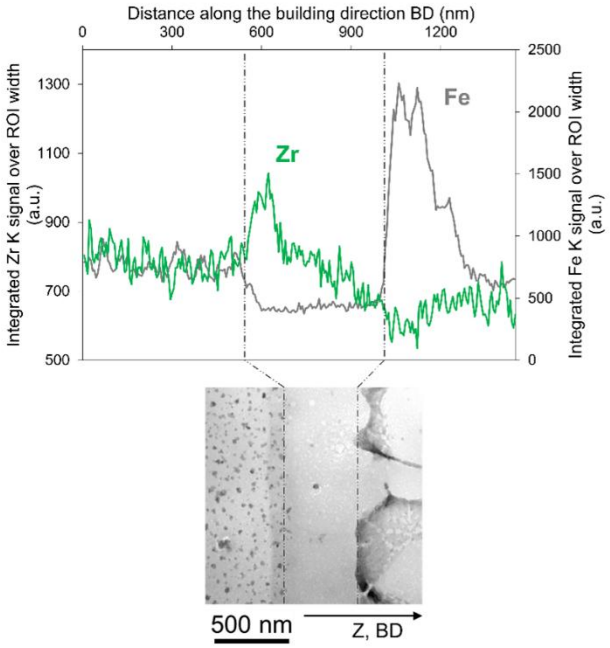

Figure 11: Integrated EDS signals for Zr and Fe over the width of the ROI displayed in insert along the building direction.

$L1_2$ Al_3Zr-induced nucleation

The formation of inoculating $L1_2$-Al_3Zr coherent particles (primary phase) is fulfilled after an incubation time (Stage I in Figure 12). The nucleation of the matrix at these particles results in the local presence of FEZ regions. The high conductivity of the present alloy is thought to be responsible for the onset of the epitaxial growth prior to the effective nucleation and growth resulting from the $L1_2$-Al_3Zr formation in the melt, at some of the locations along the MPBs. As a result of this phenomenon and the cross-section of the 3D melt pool structure, an FEZ is not systematically observed just above the MPBs, as highlighted in the EBSD maps shown in Figure 5b) and c). The variation in grain growth direction, sometimes across several layers, is attributed to the epitaxial growth at locations where the solidification conditions did not enable the nucleation and growth of the $L1_2$-Al_3Zr metastable primary phase, but where the thermal gradient direction still changed significantly.

It should be pointed out that the present study reports a FEZ fraction of about 2%, while the previous work on this alloy outlined a fraction of the order of 10-20% [18]. As the processing conditions and characterization methods are comparable in both studies, this difference may be owing to variation in trace elements between the two powder batches employed. In particular, Ti is an element known to have a high growth restriction factor in Al [61], and is present for 460 ppm in the present material, compared to only 90 ppm in previous one. This hypothesis needs further experimental validation on multiple powder batches.

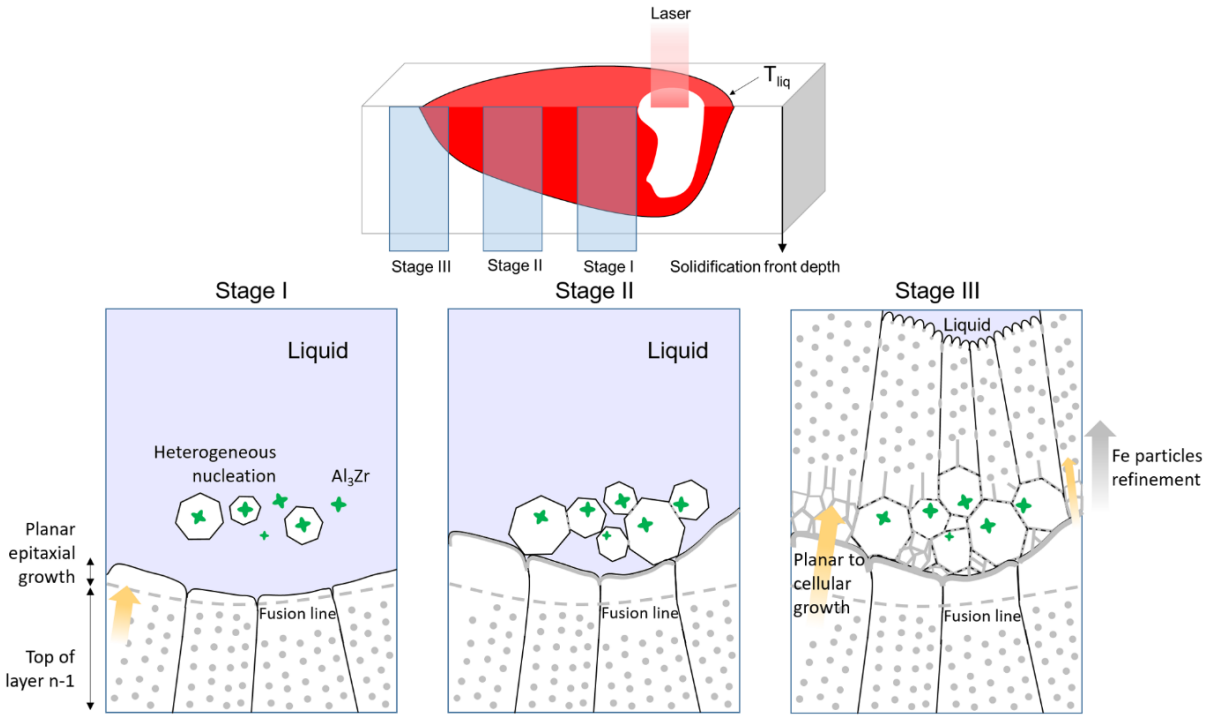

Figure 12: Microstructure development upon solidification: Stage I is the beginning of the epitaxial growth on the previously formed columnar grains while Al nuclei are formed on the Al_3Zr primary particles. Stage II highlights the competition of the two growth mechanisms as the solidification front advances. Stage III shows the columnar grain growth at lower solidification depth while the Fe rich particles refine from a continuous network above the planar front to individual globular particles within the columnar grains.

Solidification velocity-dependent partition coefficient

With increasing R towards the end of solidification, the reaction time and diffusion for the eutectic formation at the intercellular regions reduce, resulting in a change of morphology from a grain boundary network of particles to finer globular particles and more Fe supersaturation within the matrix. The latter is caused by the acceleration of the S/L interface as solidification progresses and thus the reduced time available to accommodate for solute diffusion [60]. Despite being a departure from equilibrium (the total Gibbs free energy of the system is not at its lowest point), the S/L interface might still be under local equilibrium. At an even higher velocity of the S/L interface, not necessarily attained upon LPBF, atoms might be trapped by the interface and the effective partition coefficient is then equal to one, corresponding to "solute trapping". A model was proposed by Aziz [62] to depict the variation in effective partition coefficient as it varies between the two extrema, namely the equilibrium phase diagram partition coefficient k_0 and the partition coefficient upon solute trapping (equal to 1). The model [60] is often used to describe the velocity-dependent partition coefficient k_v as:

$$k_v = \frac{k_0 + Pe}{1 + Pe}$$

where Pe is the solutal Peclet number given by:

$$Pe = \frac{a_0 R}{D_l}$$

where a_0 is the width of the solute diffusion zone at the solidification front (taken as 10 nm for the simple calculations shown below) and D_l is the mass diffusivity of the solute element in the liquid. We work under the assumption that the solute diffusivity in the liquid is roughly similar to the solute diffusivity within the S/L interface, originally used by Aziz in his model. The solute diffusivity in the liquid was taken at 928K, which corresponds to the onset of the matrix nucleation from the liquid based on Thermo-Calc calculations. The diffusion of Fe is 2.5×10^{-8} m^2/s based on Table 4 in [63], and that of Zr is 6.8×10^{-10} m^2/s based on in-house ab initio molecular dynamic calculus. The equilibrium partition coefficients for both elements were taken at 928K and are 0.025 and 3.2 for Fe and Zr, respectively, calculated with Thermo-Calc for the Al-1Fe-1Zr system. One can point out these k_0 values do not vary significantly upon solidification.

One should keep in mind that this model was developed considering a planar growth front. Under this assumption the model highlights that as R increases, k_v tends to unity, see Figure 13. The overlaid range of solidification front velocities for the LPBF process from bottom to top of the melt pool also highlights the expected significant variation in Zr and Fe solute partitioning. Zr is a peritectic element with respect to Al ($k_0 > 1$), while Fe is eutectic ($k_0 < 1$). Considering the R values achieved in LPBF, see Figure 13, extended solubility, in other words supersaturation, of Fe can be expected towards the last stages of solidification. Similar predictions and experimental results for Si, which is another eutectic element ($k_0 \sim 0.13$), confirm extended solubilities under LPBF solidification conditions of an Al10Si0.3Mg [64].

The peak observed for the integrated EDS signal of Zr at the beginning of the planar growth, see Figure 13, can also be explained considering the velocity-dependent partition coefficient of this solute. Towards the end of solidification (corresponding to the CZ just below the melt pool boundary), the k_v of Zr was quite smaller than its equilibrium value. Upon solidification of the first liquid (low R), the k_v of Zr is high, hence the observed peak and decrease with the solidification progression.

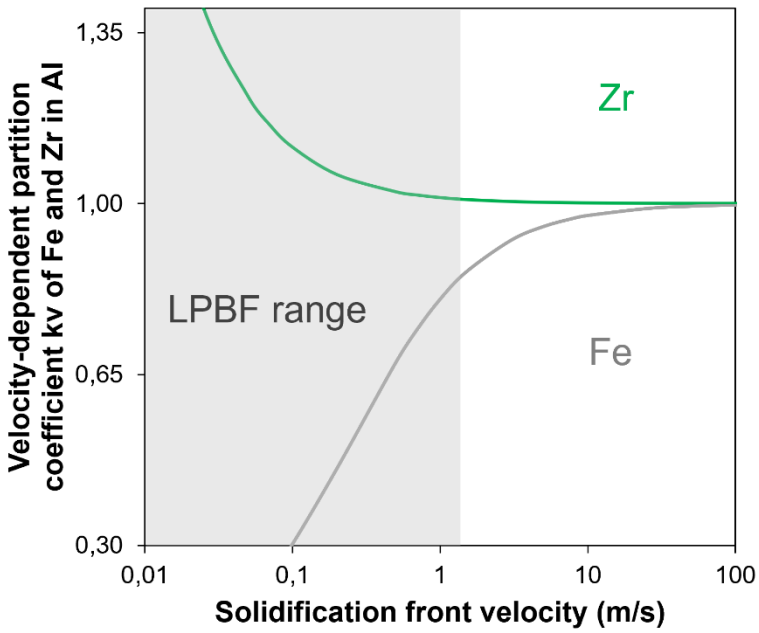

Figure 13: Estimated velocity-dependent partition coefficients of Fe and Zr in the Al-1Fe-1Zr system, based on Aziz model calculated at 925K, with equilibrium partition coefficient of 0.025 and 3.2 for Fe and Zr, respectively.

4.3. Discontinuous precipitation

Within the aged material, regions of lower indentation hardness values were highlighted by the skewed distribution presented in Figure 8d). The identification of the corresponding indents revealed the presence of an additional population of precipitates in the vicinity of few grain boundaries in the CZ and FEZ of the aged samples, see Figure 14a-c). These fan-like Zr-rich precipitates were revealed by STEM-EDS, see Figure 14d). The BF image in Figure 14d) highlights the presence of both fine and coarse Zr-rich particles. Such morphologies have already been reported by Griffiths et al. [44] in an Al-Mg-Zr alloy produced by LPBF and peak-aged at 400°C for 8h. The authors identified these precipitates as coherent $L1_2$-Al_3Zr. This is consistent with the SAED pattern obtained from a region featuring such precipitates in Figure 14e-f). Despite being seldom reported for LPBF Al alloys, this phenomenon has been extensively reviewed for aged grades obtained from other processes such as casting and melt spinning [65,66]. Typically described as discontinuous precipitation, Nes and Billdal [67] explained that it is the result of the grain boundary migration within a supersaturated solid solution of Zr. The movement of the grain boundary is associated with the loss of supersaturation and the precipitation is controlled by grain boundary diffusion. Interestingly, while the globular Fe-rich intermetallics, which formed during solidification, can be found within such areas, no faceted intermetallics from ageing are detected close to the discontinuous Al_3Zr precipitation. It suggests that the faceted $Al_{13}Fe_4$ and fan-like $L1_2$-Al_3Zr precipitation occur within a similar temperature/time range, and that these may impede each other. Additional SEM images highlight that the grain boundary migration is pinned by the coarse intergranular $Al_{13}Fe_4$, thereby limiting the extent to which discontinuous precipitation can take place, see Figure 14c). From EBSD orientation maps displayed in Figure 2a) and d), one can assert that the local grain boundary migration of a few microns results in insignificant grain growth when compared to the as-built state. High magnification EBSD in such regions shows that the growing grain orientation is conserved.

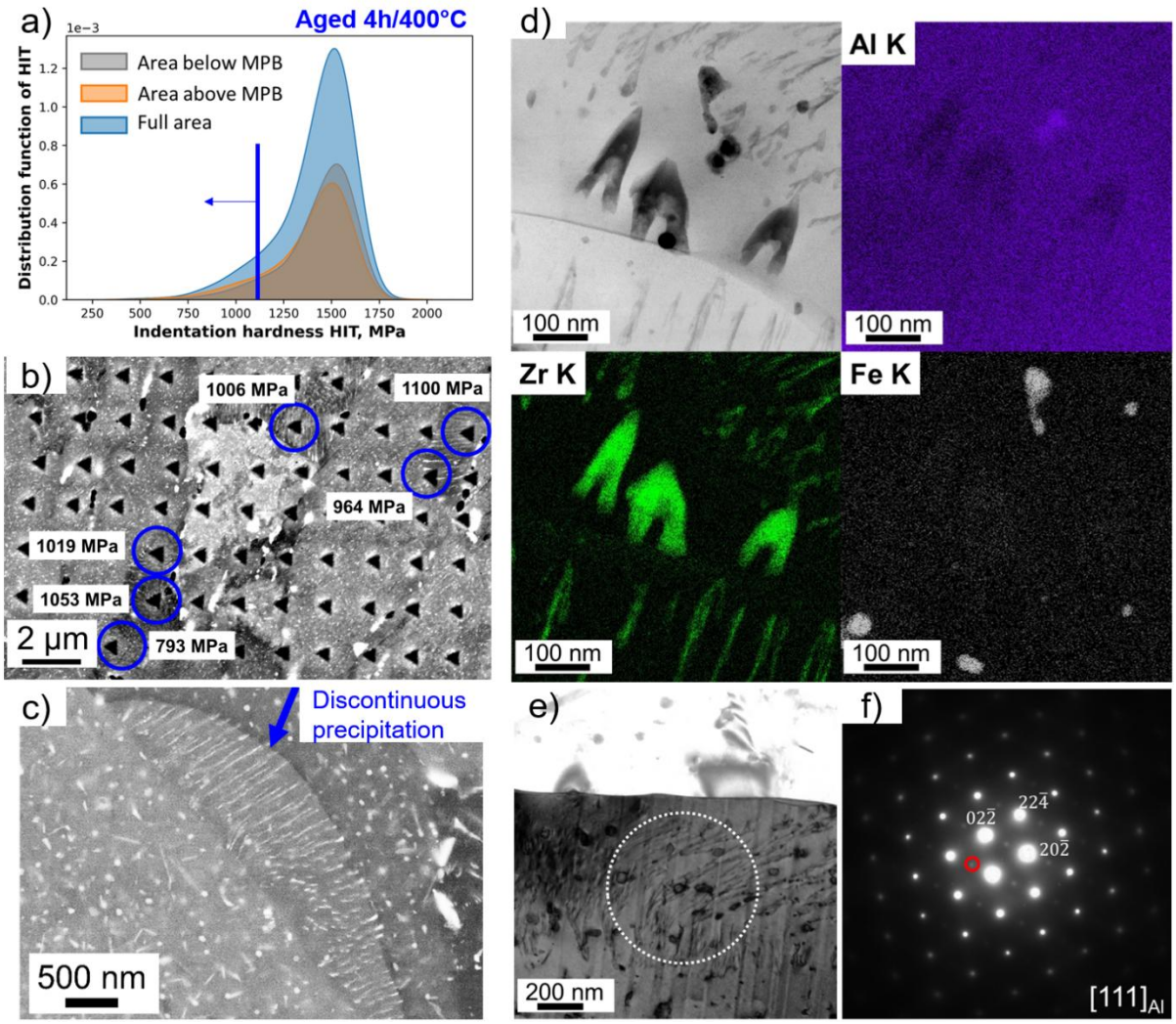

Figure 14: a) Indentation hardness distribution of the aged material skewed to the left. b) BSE image of the indented area with low hardness indents circled out and corresponding to hardness to the left of the blue line on the distribution. c) BSE image of discontinuous precipitation observed at grain boundaries typically observed at the indents circled out in b). d) BF STEM image of discontinuous $L1_2$-Al_3Zr precipitation at grain boundaries, and corresponding EDS maps of Aluminium, Zirconium and Iron. e) STEM BF image in zone axis with discontinuous precipitation and f) SAED pattern corresponding to the circular area on the BF image.

The discontinuous precipitation of coherent $L1_2$-Al_3Zr at grain boundary upon ageing means that some of the Zr remaining in the matrix is locally consumed to form these coarser precipitates instead of contributing to the continuous precipitation of the $L1_2$-Al_3Zr nanoprecipitates within the grains. It should be mentioned that discontinuous precipitation is also sometimes observed within the MPB, which is consistent with the Zr supersaturation of the MPBs in the as-built state (**Fig. S10**). Due to their large sizes, these fan-like particles do not contribute as much to the material strengthening as the $L1_2$-Al_3Zr nanoprecipitates do, hence the tail in the indentation distribution of the aged material.

The observation of the microstructure of the samples aged 1h at 400°C highlights that discontinuous precipitation is already visible at such an early stage (**Fig. S11a)**). Lowering the treatment temperature for example to 370°C requires longer treatment to compensate for

the reduced diffusivities of Zr and Fe. The equivalent time-temperature treatment considering Zr diffusion, 24 hours at 370°C, permits to achieve comparable hardness and conductivity to 4 hours at 400°C, but discontinuous precipitation is still present (see **Fig. S11b)**). Similar trials at higher temperature for shorter time did not circumvent the issue. Thus, at this stage, the treatment at 400°C for 4h remains a recommended ageing approach for high strength. Despite resulting in a small amount of local discontinuous precipitation (less than 2% based on ImageJ analysis of SEM images), this heat treatment yields an homogeneous distribution of plastic deformation, and a high strength – conductivity trade-off within a reasonably short amount of time.

4.4. Strengthening mechanisms

Strengthening in the as-built specimen

Overlaid microstructural heterogeneities are present within the melt pool with differences of grain size, precipitation and solid solution. These will result in variations of the different contributions to the alloy strengthening at the melt pool scale. Below, an attempt to evaluate the predominance of these contributions is detailed and presented in Figure 15. A precise quantitative estimate of these contributions would suffer from number of parameters that are either not properly measured or exhibiting important variability. Here, the idea is to weigh each strengthening contribution. Overall, the main contributions to the as-built strength can be summarized as: (i) grain boundary strengthening (Hall-Petch effect), (ii) solid solution strengthening, and (iii) particle strengthening. For simplicity, the contribution from residual stresses and dislocations is disregarded.

(i) The Hall-Petch relationship $\Delta\sigma_{GB} = \sigma_0 + kd^{-0.5}$ is employed with σ_0 the lattice frictional stress of pure Al (10 MPa), k the Hall-Petch slope (0.06 MPa.m$^{1/2}$ [68]), d the average grain diameter taken across the CZ and FEZ (10 µm). The grain boundary contribution is estimated to be about 30 MPa.

(ii) The solid solution strengthening $\Delta\sigma_{SS}$ is expected to contribute to some extent to the overall strength of the as-built material, as can be inferred from the velocity-dependent partition coefficients of Fe and Zr in Al, despite their low solubility in Al at equilibrium, see Figure 13. It is also suspected from the increase of conductivity from the as-built to the peak-aged state, which highlights the presence of less solute atoms in solution after ageing. As an upper boundary, we can consider that all Zr is supersaturated in solid solution (i.e., 0.3 at. %), thereby neglecting the amount of Zr consumed by the formation of primary $L1_2$-Al_3Zr. Considering that all Fe is totally consumed in the $Al_{13}Fe_4$ after ageing at 400°C/4h (the atomic fraction of the $Al_{13}Fe_4$ phase is 2.2% based on Thermo-Calc calculations under equilibrium conditions), and that the fraction of Fe-rich intermetallics in the as-built state is about two-thirds that of the aged sample (estimations based on image analysis), we can assume that about 0.2 at. % is still in solid solution. Based on the work of Uesugi and Higashi [69], the solid solution strengthening contributions of Fe and Zr can be estimated with the following equation:

$$\Delta\sigma_{ss} = M\left(\frac{3}{8}\right)^{\frac{2}{3}}\left(\frac{1+\nu}{1-\nu}\right)^{\frac{4}{3}}\left(\frac{w}{b}\right)^{\frac{1}{3}} G|\varepsilon|^{\frac{4}{3}}c^{\frac{2}{3}}$$

with M the Taylor factor (3.06), ν Poisson´s ratio (0.345), w the interaction force range ($w = 5b$, with b the Burgers vector i.e., 0.286 nm), G the shear modulus of the Al matrix (25.4 GPa), ε the misfit strains for the solute atoms (i.e., for Fe atoms -4.52% and for Zr

atoms 1.23%) and c the solute concentration. This yields a total $\Delta\sigma_{ss}$ of about 60 MPa, with 50 MPa attributed to Fe and 10 MPa from Zr.

As solidification advances, more and more solutes are expected to be saturated in solid solution. The important contribution from Fe to solid solution strengthening is therefore held responsible for the indentation hardness increase towards the top of the CZ region, just below the MPBs in the as-built state, see Figure 7c). For simplicity's sake, these solutes concentration gradients are not considered for the present global estimation.

(iii) The rest of contribution to strengthening can be partly associated to particle strengthening caused by the Fe-rich globular intermetallics observed in the as-built microstructure, to an extent of about 40 to 50 MPa, which is consistent with their relative coarse appearance. These particles may contribute by Orowan dislocation looping strengthening or through a load transfer mechanism within the composite-like microstructure.

Strengthening in the aged specimen 4h/400°C

The aged specimen is characterized by the dual precipitation of nanoprecipitates of the $L1_2$-Al_3Zr phase and faceted $Al_{13}Fe_4$ precipitates, and the associated removal of solute atoms from the matrix. Below, the contributions to strengthening in this peak-aged condition are discussed.

(i) The contribution from Hall-Petch strengthening is considered unchanged from the as-built state (~ 30 MPa), since no significant grain size variation is recorded from EBSD, despite the minor local discontinuous precipitation.

(ii) Very low concentration of solutes should remain in the matrix and the solid solution strengthening contribution can be considered negligible in that condition.

(iii) The precipitation of the coherent cubic $L1_2$-Al_3Zr nanoprecipitates is expected to contribute substantially to the strengthening of the alloy. As recalled and detailed by Li et al. [13], particle strengthening is determined by the minimum value of $\Delta\sigma_{ord}$, $\Delta\sigma_{coh} + \Delta\sigma_{mod}$ and $\Delta\sigma_{Or}$, with $\Delta\sigma_{ord}$ the order strengthening, $\Delta\sigma_{coh}$ the coherency strengthening, $\Delta\sigma_{mod}$ the modulus mismatch strengthening, and $\Delta\sigma_{Or}$ the Orowan dislocation looping strengthening. Considering a fraction of $L1_2$-Al_3Zr of 0.015 (equilibrium fraction at 400°C calculated with Thermo-Calc), an average particle radius of 2 nm, we obtain a particle strengthening contribution of about 208 MPa, owing to coherency strengthening (~ 33 MPa), and modulus mismatch strengthening (~ 175 MPa), derived from following equations [13]. The equations for the calculus of $\Delta\sigma_{ord}$ and $\Delta\sigma_{Or}$ are provided in the supplementary material.

$$\Delta\sigma_{coh} = M\alpha_{\varepsilon}(G\theta)^{\frac{3}{2}}\left(\frac{Rf}{0.5Gb}\right)^{\frac{1}{2}}$$

$$\Delta\sigma_{mod} = 0.055M(\Delta G)^{\frac{3}{2}}\left(\frac{2f}{Gb^2}\right)^{1/2} b\left(\frac{R}{b}\right)^{\frac{3m}{2}-1}$$

with α_{ε} a constant (2.6), θ the constrained lattice parameter mismatch at room temperature (0.005), f the volume fraction of particles (from Thermo-Calc), ΔG the shear modulus mismatch between the matrix and particle (31.6 MPa), R the average particle radius (estimation from TEM image) and m a constant (0.85).

The rest of the contributions to strengthening is attributed to the presence of the globular and faceted Fe-rich particles. The intragranular globular Fe-rich particles are stable upon heat treatment at 400°C for 4h, see Figure 2c)-f). Thus, it is assumed that the strengthening contribution of the globular Fe-rich intermetallics is unchanged after ageing at

400°C/4h (counting for about 40-50 MPa). However, the precipitation of the faceted Fe-rich particles upon ageing at 400°C (Figure 3) may also bring a non-negligible contribution to the yield strength. Figure 15 gives an overview of the variation of contribution to strengthening from the as-built to the peak-aged condition (4h/400°C). It appears rather clear that while solid solution strengthening contributes importantly to the as-built strength (~ 45%), the homogeneous nanoprecipitation of the $L1_2$-Al_3Zr is the major contribution to the strength of the aged specimens (more than 60%).

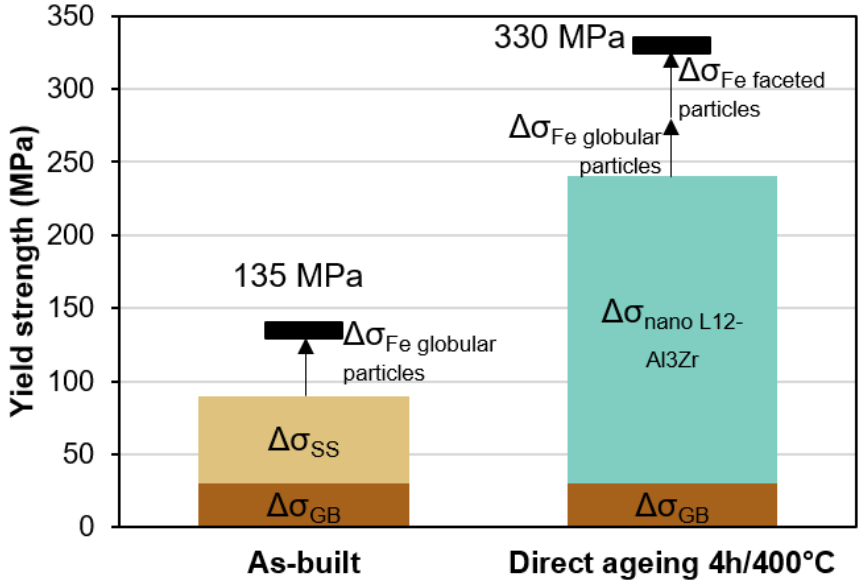

Figure 15: Estimated contributions to the strengthening of the Al-1Fe-1Zr alloy in the as-built and peak-aged conditions (4h/400°C) with $\Delta\sigma_{GB}$ the grain boundary strengthening, $\Delta\sigma_{SS}$ the solid solution strengthening, $\Delta\sigma_{Fe\ particles}$ the particle strengthening owing to the Fe-rich globular and faceted particles, $\Delta\sigma_{nano\ L12-Al3Zr}$ the particle strengthening owing to the homogeneous $L1_2$-Al_3Zr nanoprecipitation in the aged material.

Behavior of melt pool boundaries

At the MPBs, the planar growth region is characterized by an important depletion in Fe as revealed by the characterization of the as-built material. It was previously pointed out that the solid solution strengthening of the Al matrix granted by Fe surpasses that of Zr. In addition, this zone appears precipitation-free in the as-built state. Therefore, despite its small extent within the melt pool, it is expected to be a soft region within the microstructure. As MPBs are interconnected, these are likely forming an actual 3D softer network within the as-built bulk material. This is consistent with the plastic deformation map of the in situ tensile test, during which strain amplification is recorded in the MPBs vicinity. Despite this softer network of MPBs, the as-built specimen offers a high ductility also post-necking, also as evidenced from the supplementary Video of the in situ tensile test.

Such localisation of the damage at the MPBs is no longer observed in the aged specimen, consistent with the homogeneous nanoprecipitation of the $L1_2$-Al_3Zr phase evidenced throughout the microstructure, see Figure 4 and Figure 6.

5. Summary and Conclusions

The multiscale microstructural and mechanical characterization of the novel Al-1Fe-1Zr clarifies the origin of its microstructure inherited from LPBF and sheds light on the microstructure-property relationship:

- Solidification occurs by epitaxial growth from previous layers, while few primary $L1_2$-Al_3Zr particles are formed in the melt and trigger the Al heterogeneous nucleation resulting in fine equiaxed zones (FEZ).
- Epitaxy is initiated with a planar solidification front (high G, low R), leading to particle-free regions in as-built condition at the melt pool boundaries, and rather enriched in Zr, a solute known to show a peritectic behavior when alloyed with Al, while Fe is rejected ahead of the S/L interface (eutectic behavior of Fe in Al). These regions are softer, causing strain localization as seen from the in situ tensile test.
- Then the planar epitaxial front becomes unstable due to changes in solidification conditions that are more favorable for constitutional undercooling, and a cellular solidification structure is developed resulting in a network of fine Fe globular intermetallics at the cell walls.
- As solidification proceeds, R increases resulting in more Fe solute supersaturation and an increase of its solid solution strengthening contribution as observed by nanoindentation.

This complex microstructure obtained from LPBF permits through direct ageing (4h/400°C) to obtain an electrical conductivity of 27 MS/m (i.e., 45.5 % IACS), a thermal conductivity of 180 W/m·K, and yield strength of 330 MPa, via:

- Nanoprecipitation of remaining Fe and Zr solutes, increasing both conductivity and strength. Strength is in particular driven by homogeneously precipitated nanoscale $L1_2$-Al_3Zr throughout the microstructure.
- Fe-rich intermetallics decorating the grain boundaries in the as-built microstructure which limit the impact of discontinuous $L1_2$-Al_3Zr precipitation on strengthening.

As shown by the nanoindentation and in situ tensile tests, the new Al-1Fe-1Zr alloy achieves, after the 4h/400°C heat treatment, a homogeneous strain distribution throughout the melt pools, a high strength and ductility. In contrast, the melt pool boundaries play an important role for tensile strain localization in the as-built material.

Declaration of competing interests

The authors declare that they have no known competing financial interests or personal relationships that could have appeared to influence the work reported in this paper.

Acknowledgements

This work has been conducted in the framework of the Aéroprint project supported by La Région Auvergne-Rhône-Alpes. This work has benefited from the investments made by the Center of Excellence of Multifunctional Architectured Materials "CEMAM" n°AN-10-LABX-44-01. This work has benefited from the facilities available on the characterization platform CMTC of Grenoble INP-UGA. Additional thanks are addressed to the CERMAV laboratory of CNRS for granting use of their TEM equipment. The authors would also like to acknowledge the support from Constellium. Gilles Renou and Patricia Donnadieu are acknowledged for their technical support and fruitful discussions.

References

[1] L. Reijnders, Copper substitutability might be about 60% or more of current copper use, J Clean Prod. 284 (2021) 1–3. https://doi.org/https://doi.org/10.1016/j.jclepro.2020.124774.

[2] B. Vayre, F. Vignat, F. Villeneuve, Designing for additive manufacturing, Procedia CIRP. 3 (2012) 632–637. https://doi.org/10.1016/j.procir.2012.07.108.

[3] I.F. Ituarte, N. Boddeti, V. Hassani, M.L. Dunn, D.W. Rosen, Design and additive manufacture of functionally graded structures based on digital materials, Addit Manuf. 30 (2019) 1–14. https://doi.org/10.1016/j.addma.2019.100839.

[4] A. Leicht, U. Klement, E. Hryha, Effect of build geometry on the microstructural development of 316L parts produced by additive manufacturing, Mater Charact. 143 (2018) 137–143. https://doi.org/10.1016/j.matchar.2018.04.040.

[5] GE Additive, Storyboard: GE9X Additive Parts, n.d. https://www.ge.com/additive/sites/default/files/2020-08/GE9X%20Additive%20parts.pdf (accessed March 28, 2023).

[6] J.H. Martin, B.D. Yahata, J.M. Hundley, J.A. Mayer, T.A. Schaedler, T.M. Pollock, 3D printing of high-strength aluminium alloys, Nature. 549 (2017) 365–369. https://doi.org/10.1038/nature23894.

[7] A. Mehta, L. Zhou, T. Huynh, S. Park, H. Hyer, S. Song, Y. Bai, D.D. Imholte, N.E. Woolstenhulme, D.M. Wachs, Y. Sohn, Additive manufacturing and mechanical properties of the dense and crack free Zr-modified aluminum alloy 6061 fabricated by the laser-powder bed fusion, Addit Manuf. 41 (2021) 1–15. https://doi.org/10.1016/j.addma.2021.101966.

[8] M. Opprecht, J.P. Garandet, G. Roux, C. Flament, An understanding of duplex microstructures encountered during high strength aluminium alloy laser beam melting processing, Acta Mater. 215 (2021) 1–14. https://doi.org/10.1016/j.actamat.2021.117024.

[9] P. Mair, L. Kaserer, J. Braun, N. Weinberger, I. Letofsky-Papst, G. Leichtfried, Microstructure and mechanical properties of a TiB2-modified Al–Cu alloy processed by laser powder-bed fusion, Materials Science and Engineering A. 799 (2021) 1–8. https://doi.org/10.1016/j.msea.2020.140209.

[10] T. Gao, S. Zhang, G. Liu, Q. Sun, J. Liu, Q. Sun, J. Sun, Z. Wang, X. Liu, X. Wang, A high strength AlSi10Mg alloy fabricated by laser powder bed fusion with addition of Al-Ti-C-B master alloy powders, Materialia (Oxf). 16 (2021) 1–9. https://doi.org/10.1016/j.mtla.2021.101103.

[11] M. Opprecht, J.P. Garandet, G. Roux, C. Flament, M. Soulier, A solution to the hot cracking problem for aluminium alloys manufactured by laser beam melting, Acta Mater. 197 (2020) 40–53. https://doi.org/10.1016/j.actamat.2020.07.015.

[12] L. Zhou, H. Hyer, S. Park, H. Pan, Y. Bai, K.P. Rice, Y. Sohn, Microstructure and mechanical properties of Zr-modified aluminum alloy 5083 manufactured by laser powder bed fusion, Addit Manuf. 28 (2019) 485–496. https://doi.org/10.1016/j.addma.2019.05.027.

[13] R. Li, M. Wang, Z. Li, P. Cao, T. Yuan, H. Zhu, Developing a high-strength Al-Mg-Si-Sc-Zr alloy for selective laser melting: Crack-inhibiting and multiple strengthening mechanisms, Acta Mater. 193 (2020) 83–98. https://doi.org/10.1016/j.actamat.2020.03.060.

[14] J.R. Croteau, S. Griffiths, M.D. Rossell, C. Leinenbach, C. Kenel, V. Jansen, D.N. Seidman, D.C. Dunand, N.Q. Vo, Microstructure and mechanical properties of Al-Mg-Zr alloys processed by selective laser melting, Acta Mater. 153 (2018) 35–44. https://doi.org/10.1016/j.actamat.2018.04.053.

[15] M. Genc, P. Eloi, J.J. Blandin, C. Pascal, P. Donnadieu, F. De Geuser, P. Lhuissier, C. Desrayaud, G. Martin, Optimization of the strength vs. conductivity trade-off in an aluminium alloy designed for laser powder bed fusion, Materials Science and Engineering A. 858 (2022). https://doi.org/10.1016/j.msea.2022.144139.

[16] F. Leijon, S. Wachter, Z. Fu, C. Körner, S. Skjervold, J. Moverare, A novel rapid alloy development method towards powder bed additive manufacturing, demonstrated for binary Al-Ti, -Zr and -Nb alloys, Mater Des. 211 (2021) 1–17. https://doi.org/10.1016/j.matdes.2021.110129.

[17] S.Z. Uddin, L.E. Murr, C.A. Terrazas, P. Morton, D.A. Roberson, R.B. Wicker, Processing and characterization of crack-free aluminum 6061 using high-temperature heating in laser powder bed fusion additive manufacturing, Addit Manuf. 22 (2018) 405–415. https://doi.org/10.1016/j.addma.2018.05.047.

[18] C. Pauzon, M. Buttard, A. Després, B. Chehab, J.-J. Blandin, G. Martin, A novel laser powder bed fusion Al-Fe-Zr alloy for superior strength-conductivity trade-off, Scr Mater. 219 (2022) 1–7. https://doi.org/10.1016/j.scriptamat.2022.114878.

[19] S. Aksöz, Y. Ocak, N. Maraşlı, E. Çadirli, H. Kaya, U. Böyük, Dependency of the thermal and electrical conductivity on the temperature and composition of Cu in the Al based Al–Cu alloys, Exp Therm Fluid Sci. 34 (2010) 1507–1516. https://doi.org/https://doi.org/10.1016/j.expthermflusci.2010.07.015.

[20] W. Lee, J. Lee, W. Kyoung, H. Lee, H. Lee, D. Kim, Effect of inhomogeneous composition on the thermal conductivity of an Al alloy during the precipitation-hardening process, Journal of Materials Research and Technology. 9 (2020) 10139–10147. https://doi.org/10.1016/j.jmrt.2020.07.040.

[21] P.G. Klemens, R.K. Williams, Thermal conductivity of metals and alloys, International Materials Reviews. 31 (1986) 197–215. https://doi.org/10.1179/095066086790324294.

[22] L. Pan, F.A. Mirza, K. Liu, X.G. Chen, Effect of Fe-rich particles and solutes on the creep behaviour of 8xxx alloys, Materials Science and Technology (United Kingdom). 33 (2017) 1130–1137. https://doi.org/10.1080/02670836.2016.1258156.

[23] X. Qi, N. Takata, A. Suzuki, M. Kobashi, M. Kato, Change in microstructural characteristics of laser powder bed fused Al–Fe binary alloy at elevated temperature, J Mater Sci Technol. 97 (2022) 38–53. https://doi.org/10.1016/j.jmst.2021.04.038.

[24] M.T. Pérez-Prado, A. Martin, D.F. Shi, S. Milenkovic, C.M. Cepeda-Jiménez, An Al-5Fe-6Cr alloy with outstanding high temperature mechanical behavior by laser powder bed fusion, Addit Manuf. 55 (2022) 1–11. https://doi.org/10.1016/j.addma.2022.102828.

[25] S. Feng, Y. Cui, E. Liotti, A. Lui, C.M. Gourlay, P.S. Grant, In-situ X-ray radiography of twinned crystal growth of primary Al13Fe4, Scr Mater. 184 (2020) 57–62. https://doi.org/10.1016/j.scriptamat.2020.04.010.

[26] Z. Song, O. V. Magdysyuk, L. Tang, T. Sparks, B. Cai, Growth dynamics of faceted Al13Fe4 intermetallic revealed by high-speed synchrotron X-ray quantification, J Alloys Compd. 861 (2021) 1–18. https://doi.org/10.1016/j.jallcom.2021.158604.

[27] K. Liu, X. Cao, X.G. Chen, Effect of Mn, Si, and cooling rate on the formation of iron-rich intermetallics in 206 Al-Cu cast alloys, Metallurgical and Materials Transactions B. 43 (2012) 1231–1240. https://doi.org/10.1007/s11663-012-9694-7.

[28] X. Cao, J. Campbell, Morphology of β-Al5FeSi phase in Al-Si cast alloys, Mater Trans. 47 (2006) 1303–1312. https://doi.org/10.2320/matertrans.47.1303.

[29] J.A. Glerum, S. Hocine, C.S.T. Chang, C. Kenel, S. Van Petegem, N. Casati, D.F. Sanchez, H. Van Swygenhoven, D.C. Dunand, Operando X-ray diffraction study of thermal and phase evolution during laser powder bed fusion of Al-Sc-Zr elemental powder blends, Addit Manuf. 55 (2022) 102806. https://doi.org/10.1016/j.addma.2022.102806.

[30] ASTM-International, ASTM B964: Standard Test Method for Flow Rate of Metal Powders Using the Carney Funnel., 02 (2014) 20–22. https://doi.org/10.1520/B0964-09.2.

[31] F. Bachmann, R. Hielscher, H. Schaeben, Texture analysis with MTEX- Free and open source software toolbox, Solid State Phenomena. 160 (2010) 63–68. https://doi.org/10.4028/www.scientific.net/SSP.160.63.

[32] ImageJ: Image Processing and Analysis in Java, (n.d.). https://imagej.nih.gov/ij/index.html (accessed March 2, 2020).

[33] E.F. Rauch, M. Véron, Automated crystal orientation and phase mapping in TEM, Mater Charact. 98 (2014) 1–9. https://doi.org/10.1016/j.matchar.2014.08.010.

[34] M. Buttard, B. Chehab, R. Shahani, F. Robaut, G. Renou, C. Tassin, E. Rauch, P. Donnadieu, A. Deschamps, J.J. Blandin, G. Martin, Multi-scale microstuctural investigation of a new Al-Mn-Ni-Cu-Zr aluminium alloy processed by laser powder bed fusion, Materialia (Oxf). 18 (2021) 1–12. https://doi.org/10.1016/j.mtla.2021.101160.

[35] M. Buttard, G. Martin, X. Bataillon, G. Renou, P. Lhuissier, J. Vilanova, B. Chehab, P. Jarry, J.-J.J. Blandin, P. Donnadieu, J. Villanova, B. Chehab, P. Jarry, J.-J.J. Blandin, P. Donnadieu, Towards an alloy design strategy by tuning liquid local ordering: what solidification of an Al-alloy designed for laser powder bed fusion teaches us, Addit Manuf. 61 (2023) 1–18. https://doi.org/10.1016/j.addma.2022.103313.

[36] A. Després, C. Mayer, M. Veron, E.F. Rauch, M. Bugnet, J.J. Blandin, G. Renou, C. Tassin, P. Donnadieu, G. Martin, On the variety and formation sequence of second-phase particles in nickel-based superalloys fabricated by laser powder bed fusion, Materialia (Oxf). 15 (2021) 1–13. https://doi.org/10.1016/j.mtla.2021.101037.

[37] A. Després, S. Antonov, C. Mayer, M. Veron, E.F. Rauch, C. Tassin, J.-J. Blandin, P. Kontis, G. Martin, Revealing the true partitioning character of zirconium in additively manufactured polycrystalline superalloys, Additive Manufacturing Letters. 1 (2021) 100011. https://doi.org/10.1016/j.addlet.2021.100011.

[38] W.C. Oliver, G.M. Pharr, An improved technique for determining hardness and elastic modulus using load and displacement sensing indentation experiments, J Mater Res. 7 (1992) 1564–1583.

[39] T. Dessolier, G. Martin, P. Lhuissier, C. Josserond, F. Roussel, F. Charlot, J.-J. Blandin, L. Maniguet, Conducting Controlled In Situ High Temperature Tensile Tests within a SEM, 2018.

[40] C. de Formanoir, G. Martin, F. Prima, S.Y.P. Allain, T. Dessolier, F. Sun, S. Vivès, B. Hary, Y. Bréchet, S. Godet, Micromechanical behavior and thermal stability of a dual-phase α+α' titanium alloy produced by additive manufacturing, Acta Mater. 162 (2019) 149–162. https://doi.org/10.1016/j.actamat.2018.09.050.

[41] A. Lechartier, G. Martin, S. Comby, F. Roussel-Dherbey, A. Deschamps, M. Mantel, N. Meyer, M. Verdier, M. Veron, Influence of the Martensitic Transformation on the Microscale Plastic Strain Heterogeneities in a Duplex Stainless Steel, Metallurgical and Materials Transactions A. 28 (2017) 20–25. https://doi.org/ttps://doi.org/10.1007/s11661-016-3858-z.

[42] F. Mas, G. Martin, P. Lhuissier, Y. Bréchet, C. Tassin, F. Roch, P. Todeschini, A. Simar, Heterogeneities in local plastic flow behavior in a dissimilar weld between low-alloy steel and stainless steel, Materials Science and Engineering: A. 667 (2016) 156–170. https://doi.org/https://doi.org/10.1016/j.msea.2016.04.082.

[43] S. Węglarczyk, Kernel density estimation and its application, in: ITM Web of Conferences, 2018: pp. 102–107. https://doi.org/https://doi.org/10.1051/itmconf/20182300037.

[44] S. Griffiths, J.R. Croteau, M.D. Rossell, R. Erni, A. De Luca, N.Q. Vo, D.C. Dunand, C. Leinenbach, Coarsening- and creep resistance of precipitation-strengthened Al–Mg–Zr alloys processed by selective laser melting, Acta Mater. 188 (2020) 192–202. https://doi.org/10.1016/j.actamat.2020.02.008.

[45] A.B. Spierings, K. Dawson, P.J. Uggowitzer, K. Wegener, Influence of SLM scan-speed on microstructure, precipitation of Al3Sc particles and mechanical properties in Sc- and Zr-modified Al-Mg alloys, Mater Des. 140 (2018) 134–143. https://doi.org/10.1016/j.matdes.2017.11.053.

[46] Q. Jia, P. Rometsch, P. Kürnsteiner, Q. Chao, A. Huang, M. Weyland, L. Bourgeois, X. Wu, Selective laser melting of a high strength Al-Mn-Sc alloy: Alloy design and strengthening mechanisms, Acta Mater. 171 (2019) 108–118. https://doi.org/10.1016/j.actamat.2019.04.014.

[47] N. Ryumt, The influence of a precipitate-free zone on the mechanical properties of an Al-Mg-Zn alloy, Acta Metallurgica. 16 (1968) 327–332.

[48] P.N.T. Unwin, G.W. Lorimer, R.B. Nicholson, The origin of the grain boundary precipitate free zone, Acta Metallurgica. 17 (1969) 1363–1377.

[49] X. Qi, N. Takata, A. Suzuki, M. Kobashi, M. Kato, Controllable tensile performance of additively manufactured Al–Fe alloy, Materials Science and Engineering A. 855 (2022) 1–10. https://doi.org/10.1016/j.msea.2022.143893.

[50] Granta Design, Granta: CES Selector materials selection software - Material level 2, (2022). https://www.grantadesign.com/products/ces/.

[51] EOS GmbH, EOS Aluminium AlSi10Mg Material Data Sheet EOS Aluminium AlSi10Mg Good Strength & Dynamic Load Bearing Capacity, 2022.

[52] X. Qi, N. Takata, A. Suzuki, M. Kobashi, M. Kato, Managing both high strength and thermal conductivity of a laser powder bed fused Al–2.5Fe binary alloy: Effect of annealing on microstructure, Materials Science and Engineering A. 805 (2021) 1–16. https://doi.org/10.1016/j.msea.2020.140591.

[53] X. Zhang, B. Mao, L. Mushongera, J. Kundin, Y. Liao, Laser powder bed fusion of titanium aluminides: An investigation on site-specific microstructure evolution

mechanism, Mater Des. 201 (2021) 1–14. https://doi.org/10.1016/j.matdes.2021.109501.

[54] P. Van Cauwenbergh, V. Samaee, L. Thijs, J. Nejezchlebová, P. Sedlák, A. Iveković, D. Schryvers, B. Van Hooreweder, K. Vanmeensel, Unravelling the multi-scale structure–property relationship of laser powder bed fusion processed and heat-treated AlSi10Mg, Sci Rep. 11 (2021) 1–15. https://doi.org/10.1038/s41598-021-85047-2.

[55] S.A. David, S.S. Babu, J.M. Vitek, Welding: Solidification and microstructure, JOM. 55 (2003) 14–20. https://doi.org/https://doi.org/10.1007/s11837-003-0134-7.

[56] B. Mondal, M. Gao, T.A. Palmer, T. DebRoy, Solidification cracking of a nickel alloy during high-power keyhole mode laser welding, J Mater Process Technol. 305 (2022). https://doi.org/https://doi.org/10.1016/j.jmatprotec.2022.117576.

[57] S. Dépinoy, Influence of solidification conditions on chemical heterogeneities and dislocations patterning in additively manufactured 316L stainless steel, Materialia (Oxf). 24 (2022) 1–14. https://doi.org/10.1016/j.mtla.2022.101472.

[58] Z. Zhu, X. Ma, P. Jiang, G. Mi, C. Wang, Planar-cellular-dendritic transformation in the fusion zone of a GH909 superalloy weldment, Journal of Materials Research and Technology. 10 (2021) 960–975. https://doi.org/10.1016/j.jmrt.2020.12.033.

[59] M. Gremaud, M. Carrard, W. Kurz, The microstructure of rapidly solidified Al-Fe subjected to laser surface treatment, Acta Metallurgica Materialia. 38 (1990) 2587–2599.

[60] T.E. Quested, A.T. Dinsdale, A.L. Greer, Thermodynamic modelling of growth-restriction effects in aluminium alloys, Acta Mater. 53 (2005) 1323–1334. https://doi.org/10.1016/j.actamat.2004.11.024.

[61] J.A. Dantzig, M. Rappaz, Solidification, First edition, Lausanne, 2009.

[62] M.J. Aziz, Model for solute redistribution during rapid solidification, J Appl Phys. 53 (1982) 1158–1168. https://doi.org/10.1063/1.329867.

[63] Y. Du, Y.A. Chang, B. Huang, W. Gong, Z. Jin, H. Xu, Z. Yuan, Y. Liu, Y. He, F.Y. Xie, Diffusion coefficients of some solutes in fcc and liquid Al: Critical evaluation and correlation, Materials Science and Engineering A. 363 (2003) 140–151. https://doi.org/10.1016/S0921-5093(03)00624-5.

[64] N. Takata, M. Liu, H. Kodaira, A. Suzuki, M. Kobashi, Anomalous strengthening by supersaturated solid solutions of selectively laser melted Al–Si-based alloys, Addit Manuf. 33 (2020) 1–11. https://doi.org/10.1016/j.addma.2020.101152.

[65] P. Málek, M. Janecek, B. Smola, P. Bartuška, J. Plestil, Structure and properties of rapidly solidified Al-Zr-Ti alloys, J Mater Sci. (2000) 2625–2633.

[66] Y.C. Chen, M.E. Fine, J.R. Weertman, Microstructural evolution and mechanical properties of rapidly solidified Al-Zr-V alloys at high temperatures, Acta Metallurgica Et Materialia. 38 (1990) 771–780.

[67] E. Nes, H. Billdal, The mechanism of discontinuous precipitation of the metastable Al3Zr phase from an Al-Zr solid solution, Acta Metallurgica. 25 (1977) 1039–1046.

[68] S. Thangaraju, M. Heilmaier, B.S. Murty, S.S. Vadlamani, On the estimation of true hall-Petch constants and their role on the superposition law exponent in al alloys, Adv Eng Mater. 14 (2012) 892–897. https://doi.org/10.1002/adem.201200114.

[69] T. Uesugi, K. Higashi, First-principles studies on lattice constants and local lattice distortions in solid solution aluminum alloys, Comput Mater Sci. 67 (2013) 1–10. https://doi.org/10.1016/j.commatsci.2012.08.037.